Journal of the European Ceramic Society 41 (2021) 6087–6114

Contents lists available at ScienceDirect

Journal of the European Ceramic Society

journal homepage: www.elsevier.com/locate/jeurceramsoc

Review article

Direct laser additive manufacturing of high performance oxide ceramics: A state-of-the-art review

Stefan Pfeiffer [a,b,*,1], Kevin Florio [c,**,1], Dario Puccio [d], Marco Grasso [d], Bianca Maria Colosimo [d], Christos G. Aneziris [b], Konrad Wegener [c], Thomas Graule [a,b]

[a] Laboratory for High Performance Ceramics, Empa – Swiss Federal Laboratories for Materials Science and Technology, Überlandstrasse 129, 8600 Dübendorf, Switzerland
[b] Institute of Ceramic, Glass and Construction Materials, TU Bergakademie Freiberg, Agricolastraße 17, 09599 Freiberg, Germany
[c] Institute of Machine Tools and Manufacturing, ETH Zürich, Leonhardstrasse 21, 8092 Zurich, Switzerland
[d] Department of Mechanical Engineering, Politecnico di Milano, via La Masa 1, 20156 Milan, Italy

ARTICLE INFO

Keywords:
Additive manufacturing
Ceramic oxides
Powder bed fusion – laser beam
Selective laser melting and sintering
Directed energy deposition

ABSTRACT

The implementation of additive manufacturing for ceramics is more challenging than for other material classes, since most of the shaping methods require polymer binder. Laser additive manufacturing (LAM) could offer a new binder-free consolidation route, since it is capable of processing ceramics in a direct manner without post-processing. However, laser processing of ceramics, especially high performance oxide ceramics, is limited by low thermal shock resistance, weak densification and low light absorptance at room temperature; particularly in the visible or near-infrared range. An extensive review focusing only on LAM (powder bed fusion – laser beam and directed energy deposition) of high performance oxide ceramics is currently lacking. This state-of-the-art review gives a detailed summary and critical analysis about process technologies, part properties, open challenges and process monitoring in the field of oxide ceramics. Improvements in accuracy and mechanical strength are proposed that could open LAM of oxide ceramics to new fields.

1. Introduction

Additive manufacturing (AM) is predicted to have a major influence on several industries in the future. It evolved from a rapid prototyping technology to produce physical models to a manufacturing technology today, which is capable to produce functional parts in a wide range of materials [1]. AM will facilitate entire new production and business strategies and open new uses and markets, since it broadens the range of products with those that can only be produced additively. In 2019, the volume of sales of products and services in AM was $11.9 billion, and the average growth was 23.3 % in the past 4 years [1,2]. Polymers have by far the biggest market share, whereas ceramics only appear as a niche, accounting for less than 2% of the total AM material sales [2,3].

Laser Additive Manufacturing (LAM) is one of the various possibilities to process materials additively. For metals and polymers, this method is already established in the industry. For oxide ceramics, the issues of low thermal shock resistance, weak densification during processing and strongly temperature-dependend absorptance [4,5] of YAG laser light (used by most commercial PBF machines because of their reliability and small spot size) hinder a broader distribution. Different approaches, such as the use of different lasers (CO_2 [6–9], pulsed Nd-YAG [10,11], high power diode [12] or femtosecond lasers [13]), various laser scanning strategies (circular [14], single-track, zigzag or island scanning strategies [15] or directed energy deposition [16,17]), preheating (microwaves [18], second laser [19,20] or within a vertical tube furnace [9]), different laser parameters [21] and formation of an amorphous phase [6,7,10,11] were considered to improve the properties of the laser manufactured ceramic components. Until now, none of these approaches proved to combine high geometrical accuracy, good mechanical properties, and extended design freedom. Furthermore, not only the laser process parameters and processing conditions should be considered, but also powder properties, such as melting temperature,

* Corresponding author at: Laboratory for High Performance Ceramics, Empa – Swiss Federal Laboratories for Materials Science and Technology, Überlandstrasse 129, 8600 Dübendorf, Switzerland.
** Corresponding author at: Institute of Machine Tools and Manufacturing, ETH Zürich, Leonhardstrasse 21, 8092 Zurich, Switzerland.
E-mail addresses: stefan.pfeiffer@empa.ch (S. Pfeiffer), florio@iwf.mavt.ethz.ch (K. Florio).
[1] Stefan Pfeiffer and Kevin Florio contribute equally to this paper.

https://doi.org/10.1016/j.jeurceramsoc.2021.05.035
Received 8 April 2021; Received in revised form 13 May 2021; Accepted 17 May 2021
Available online 19 May 2021

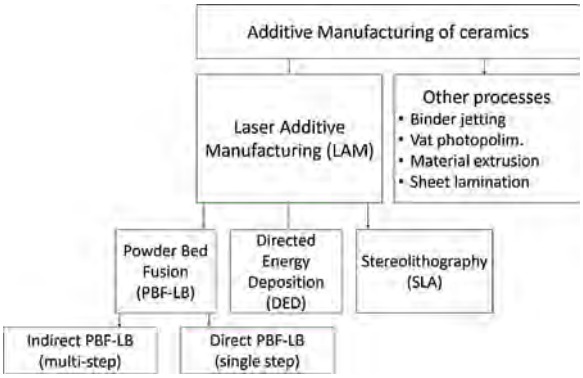

Fig. 1. Current additive manufacturing methods for ceramics in accordance to ISO/ASTM 52900:2018 and [1,3,33]; process categories highlighted in green are the ones reviewed in this study. (For interpretation of the references to colour in this figure legend, the reader is referred to the web version of this article).

absorptance [22], flowability and powder bed density [23,24] of the different oxides. In terms of powder bed absorptance of visible and near-infrared, carbon [25–29] and carbides [28] were tested as additives to increase the absorptance of the utilized oxide powders. Other works used colored oxide nanoparticles as doping to improve the laser-powder interaction [22,30–32].

The scientific literature on AM processes for ceramic materials was reviewed in previous studies [24,33–37]. Some of them were published in 2013 and 2014 [24,33,35], but since then several advances and novel solutions have been presented, tested and validated. The most recent reviews were either focused on a single type of AM process [36–38] or on a general overview of all AM processes that can be used to produce ceramic parts [34,39]. The present review has been conceived to provide a different perspective based on three main contributions that are believed to be of interest for the AM and ceramic material processing communities. First, it specifically addresses LAM processes, including both powder bed fusion and direct material deposition (directed energy deposition) technologies, for high performance oxide ceramics. In this field, a detailed classification of available methods, their pros and cons, together with their industrial potentials and open issues is presented. Second, a special focus is devoted to major issues and relevant technological aspects that were not deepened in previous studies, i.e., the mechanical characterization of manufactured parts and their defectiveness, the causes of material discontinuities and flaws and the detectability of anomalies via in-situ sensing and monitoring. Third, due to the very fast evolution of methods and technologies in this field, the present review is aimed at providing an up-to-date discussion of most recent advances and a comprehensive picture of on-going and future research streams.

2. Laser Additive Manufacturing of ceramics: classification of methods and process description

AM offers the possibility to combine the geometrical design of a part with the materials design, which in consequence can reduce the fabrication time and the unit cost for a part with specific required properties, compositions, microstructure and shape. The different AM techniques currently available for ceramics are summarized and classified in the ISO/ASTM 52900:2018 standard [40] and by different authors [1,3,33]. Several different nomenclatures have been used in the literature. In this study, we refer to the standard terminology defined in the ISO/ASTM 52900:2018 standard. A first classification can be done between single-step and multi-step AM processes. Single-step methods (also known as “direct” methods) allow the production of the part with desired geometry and material properties in one operation. Multi-step methods (also known as “indirect”) involve sequential operations.

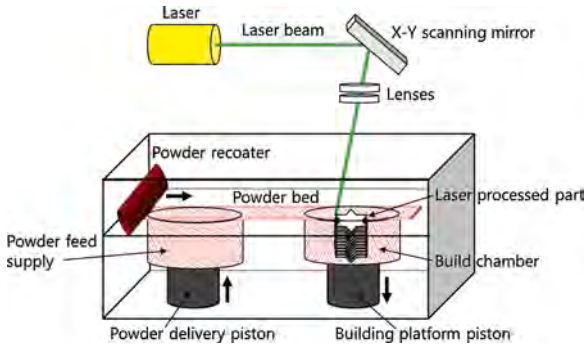

Fig. 2. Schematic of powder bed fusion with a laser beam (PBF-LB).

Commonly, the first operation is needed to obtain a given geometry, whereas the second step is aimed at consolidating the part to achieve target material properties.

Fig. 1 shows a schematic classification of AM methods for ceramics into LAM, binder jetting, VAT photopolymerization, material extrusion and sheet lamination. LAM processes for ceramics can be further classified into powder bed fusion – laser beam (PBF-LB) and Directed Energy Deposition (DED) with laser source, also known as Direct Material Deposition. PBF-LB of ceramics may involve two different underlying AM principles, i.e., direct and indirect PBF-LB. This review focuses only on the direct LAM processes, i.e., direct PBF-LB and DED.

2.1. Basic process principles

Laser-based Powder bed fusion (PBF-LB) was first developed for polymers in the 1980s by Carl R. Deckard and Joseph J. Beaman at the University of Texas [41]. In this process, particles within a powder bed are selectively fused or sintered together by employing the focused energy of a laser beam based on selective sintering or melting the material based on cross-sectional slice information to produce complex 3D parts in a layer-wise manner (layer thickness typically below 100 microns) [33,42].

Fig. 2 illustrates the schematic of PBF-LB. A typical PBF-LB-machine consists of two chambers. One is filled with the powder supply, which is spread by a powder recoater to a powder layer on the build chamber. To manufacture the part, the laser beam is guided across the powder bed of the build chamber by a scanning system, usually a galvano scanner, fusing the powder layer by layer.

In PBF-LB highly dense powder beds are required for the successful consolidation [24,43]. Furthermore, traditionally only fine-grained ceramic parts show adequate mechanical properties at room temperature, particles with sizes in the range of tens of nanometers to a few micrometers are preferred. However, particles below 10 microns tend to agglomerate [44] reducing the flowability, causing poor powder bed density and inhomogeneity. The reason is that the gravitational force dominates for bigger particles, since it scales with the third power of the diameter, whereas interparticle forces depending on particle surface only scale with the second power [42,44].

Instead of layering granules or powders, a ceramic slurry can be deposited by a doctor blade comparable to tape casting. The layers are dried subsequently. This technique was originally patented in the year 2004 [45] and it is called here slurry-based PBF-LB. As for the powder-based method, the laser beam is guided across the powder bed by a scanning system to consolidate a part based on the CAD data. The main advantages are thin layers (down to 10 μm) composed of nanoparticles that can be deposited uniformly and with a high packing density.

The formation is comparable to slip casting. Capillary forces (additional to gravitational and interparticle forces in the powder bed method) draw the liquid of the suspension into the pores of the

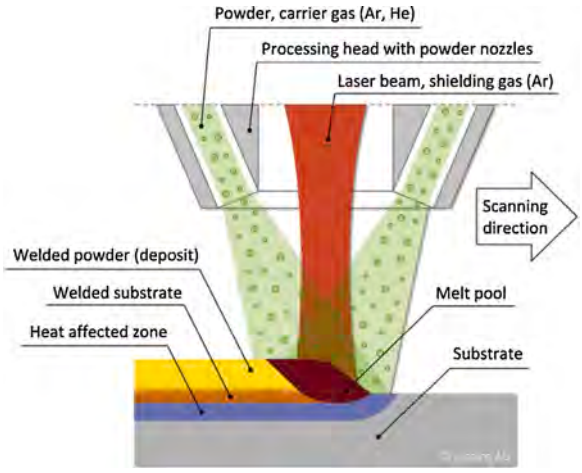

Fig. 3. Schematic of directed energy deposition according to Wirth et al. [46].

previously deposited non-solidified powder bed [6,42]. The highly dense powder bed formation is additionally assisted by the drying of the deposited slurry on a preheated building platform. For water-based slurries, this drying can be achieved in less than 10 s [7]. The speed of the doctor blade is crucial for this process. When too slow, collision between cast and doctor blade can happen due to rapid solidification of the slurry in front of the blade due to evaporation. When the solidified cast grows higher than the tailing edge of the doctor blade, collision will happen, which is especially a problem for high solid content and for slurries with finer particles (< 1 μm). When speed is too high, inhomogeneous deposition occurs due to shear stresses. Disadvantages of this layering process are the necessary removal of the parts after PBF-LB by a solvent (for water-based slurries water acts as a solvent), since the part is embedded into the densified slurry, in contrary to the powder-based method [42].

In comparison to other PBF-LB techniques, the drying step requires additional time for layering and process optimization. Furthermore, nanoparticles in multimodal powder combinations can tend to the top surface of the layer due to evaporation forces. Finally, the risk for laser processing of flammable residual solvents cannot be totally excluded, when using organic solvents [6].

A different LAM approach suitable to produce ceramic parts is directed energy deposition (DED) with laser source (also called Laser engineered net shaping in ceramics). A schematic of the process is shown in Fig. 3. DED is based on a melt pool formation by irradiation of the substrate and subsequent powder addition into the molten pool by a powder nozzle coupled to the laser beam. The desired material is transported together with an inert gas, which acts as shielding gas. Due to high deposition rates, big parts with a high density can be easily produced by this method: in general, spot diameters and layer thickness are one order of magnitude larger than in PBF-LB. Furthermore, it is possible to work with several powder streams filled with different materials to produce for example multi-material systems.

2.2. Advantages of LAM processes in comparison to other AM processes

LAM offers several possible advantages for the production of ceramic parts compared not only to traditional manufacturing processes but also to other AM methods.

- Low unit cost in LAM for small series and prototypes
- Expanded boundaries for design engineers
- Production on demand with short lead times
- Avoidance of the problematic thermal post-processing
- Possibility of merging hard-machining or laser subtractive processes with AM as a hybrid

The unit cost of a LAM part depends on material cost, build time, energy consumption, labor and indirect costs [47], which can be in general related to production volume or the degree of complexity and customization of the part (Fig. 4) [1,48]. The advantage of low unit cost in LAM for small series and prototypes, will reduce the need to produce small lots of parts in low-wage countries in the future [49]. In general, LAM requires less workforce to produce parts [50] and low raw material costs will be reached, when it can be bought commercially and further processed with a minimum effort [42].

For larger production volumes, the production via AM is favorable for complex parts (Fig. 4). For LAM increasing part complexity does not correlate with higher manufacturing costs enabling a higher degree of customization [1,42,48]. This could be particularly beneficial for the medical industry, where low volume and personalized parts are required [51] such as dental crowns, artificial limbs and porous bone scaffolds [50]. Some geometries can be built with LAM and could not be manufactured with indirect AM processes: for example parts with large wall thicknesses can lead to extremely long or even impossible debinding in indirect AM [52], but they are not problematic for LAM.

The magnitude of the potential design benefits depends in general on the application and have still not been completely exploited [42,53]. This includes the possibility to design multi-material systems [42], multifunctional components [3] and free moving parts that are directly assembled after printing (e.g. fully functional ball bearings) [50]. In the case of multi-materials, thermal expansion coefficients and shrinkage behavior of the different materials should be taken into account to avoid cracking and delamination. Furthermore, complex shaped-porous structures can be produced with a precise control of dimension, shape and amount of pores [42], which could be beneficial for several ceramic

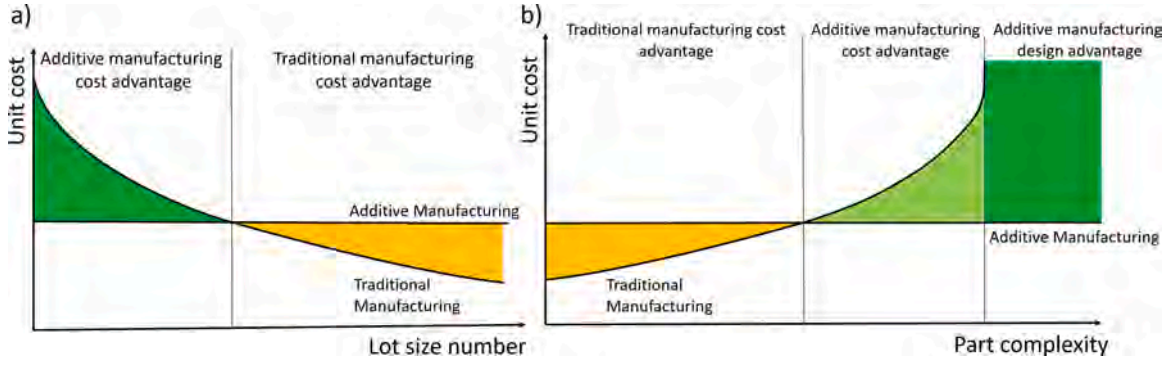

Fig. 4. Unit cost for additive and traditional manufactured parts referred to a) production volume and b) complexity or customization of the parts and influence of new design opportunities by additive manufacturing on unit cost referred to complexity of the parts compared to traditional processes. The green area shows the more favorable range for AM as manufacturing method.

applications such for example bone scaffolding and filtration membranes [3].

LAM allows the production on demand with short lead times which can result in storage costs reduction, better customer services and savings on unnecessary transportation costs. A shortened time span between design, testing and implementation leads to short lead and setup times for tooling. This reduces the time to market costs, which was one of the initial motivations for the development of rapid prototyping technologies [1,42,53].

Besides the costs considerations, the main advantage of direct consolidation of the material via LAM in comparison to other AM technologies is that the manufacturing and material fusion are combined into one-step and a time consuming thermal treatment step is not needed. Debinding and sintering in indirect AM are often based on experience and can vary considerably between different material, crystalline phase, size of the powder and component geometries. The amount of organic binder used in indirect AM methods for ceramic processing can be for example up to 50 Vol% (VAT Photopolymerization) [54]. Cracking and delamination are possible problems generated by debinding of these high organic amounts.. In addition, the avoidance of debinding and thermal treatment lead to less pollution and greenhouse emissions [55].

In contrast to other indirect AM methods, lasers offer also the possibility to merge hard machining or laser subtractive processes with AM processes as a hybrid, which presents a great chance to manufacture innovative components and broadens greatly the range of producible parts.

2.3. Challenges of LAM

Until now, several barriers prevent a broader application of LAM. Following disadvantages are specified in this subchapter:

- Low production speed and throughput
- Poor surface quality and strength issues
- High production costs for small lots, prototyps or complex-shaped parts due to expensive starting materials and high investment prices.
- Lack of technical standards, quality assurance systems and guidelines

Another drawback for LAM is the low production speed and low throughput, which limits the production of large sized objects due the long time required to build a part layer by layer [1,50,53,55,56]. The industrial usage of LAM depends on the possibility to produce parts as close as possible to the desired geometry [33], since machining can amount up to 80 % of the overall traditional manufacturing costs [57]. The surface quality is not only important for aesthetical reasons, but also can influence the mechanical properties of the printed part in AM [42]. The so-called "staircase" effect due to layer-wise production could be minimized by decreasing the layer thickness or by combination with subtractive methods. but this has negative consequences in production time and costs [33]. Since melting and rapid solidification at high temperatures are always involved in LAM, surface quality and part accuracy are challenges due to melt-pool instabilities.

Thermal stresses are generated due to the temperature gradients in LAM, which can lead to cracking. Balling, porosity and other defects due to melt-pool physics combined with a low fracture toughness of the material are typical challenges of LAM [3]. The crack problem correlates also with an increased density, since dense parts lead to a larger buildup of stresses during cooling. For a successful integration of an AM process into an existing process chain in ceramics, the finally produced part properties should be equal or superior compared to those of traditionally manufactured parts. In ceramics, each defect can cause a catastrophic failure of the ceramic component.

The high prices for specially customized raw materials will automatically reduce in the future by the economics of scale, when more competitors will enter the market [53,58]. For laser technology, the high production costs should decrease in the future due to technological improvements such as growing laser power, adoption of multiple laser and lower machine prices [53].

The lack of technical standards, quality assurance systems, manufacturing guidelines (e.g. about support design [56]), design rules and the existing patent law results in long certification periods for critical parts [59,60] and slows down a broader use of LAM for ceramic parts [1,53].

3. State of the art: materials, methods, applications

3.1. Powder bed fusion - laser beam (PBF-LB)

3.1.1. Powder bed preparation and impact on the process

In general, high performance oxide ceramics are densified by solid state sintering, which is based on diffusion processes. It is stated that high powder bed densities are necessary to overcome the obstacle of weak densification and to achieve a high density of the final parts in PBF-LB [23,24] and it is well known that strength of ceramic parts decrease with increasing porosity [61].

Different approaches to overcome the low powder bed density are as follow:

A Use of spray dried granules and mechanical blending
B Mechanical powder bed compaction
C Slurry casting via doctor blade or rubber scrapper
D Application via spraying techniques
E Electrophoretic deposition of ceramic dispersions

A. Use of spray dried granules and mechanical blending

In traditional ceramic manufacturing (e.g. pressing) the voids between and within the granules are closed by crushing and sintering [62]. However, in PBF-LB, a partial melting or total melting of the granules during laser processing is necessary, to close the voids formed by the granules. A successful application was shown by Juste et al. [25]. Aluminum oxide was mixed with additional carbon to advance the interaction between the laser and the ceramic powder, since alumina shows almost no absorption at the emitted wavelength (1070 nm) of the fiber laser light. The resultant mixture was formed by spray granulation of fine alumina powder (d_{50} of 0.4 µm) with a colloidal suspension containing graphite in the slurry to obtain highly flowable granules ensuring a dense powder bed. At a concentration of 0.1 and 1 vol% graphite, the powder showed an absorbance in a 5 mm thick pellet of about 50 % and 80 %, respectively. Sieving of the granules to reduce the layer thickness of the powder bed improved the microstructure and increased the density of the final parts.

Manganese oxide and iron oxide doped granules were also used in PBF-LB to produce alumina parts by green nanosecond-pulsed laser (wavelength of 532 nm) [22,30,32]. The necessary doping amount for a successful part consolidation was in both cases below 1 vol% due to homogeneous distribution of the colored metal oxide nanoparticles within the spray-dried granules [32,63]. The powder absorptance of the granules could be improved by incorporation of the nano-dopants up to 80.9 % in comparison to undoped granules [32]. By thermal pre-treatment of the granules tapped powder densities of up to 56.4 % of the theoretical density were reached. The hypothesis of McGeary [64], that a bimodal distribution of coarse and fine particles should give the highest packing density, could be confirmed for spray dried granules [30]. Similarly, Mapar et al. [65,66] used spray dried granules made from the eutectic composition of micron Al_2O_3 and nano yttria stabilized ZrO_2 (37 mol%). In comparison to larger granules supplied from industry, the spray dried granules showed a lower flowability, and were therefore expected to be less suitable for the PBF-LB. It was also suggested to remove the organic of the granules (at 600 °C) before the laser treatment [66]. Furthermore, Liu et al. [67] showed the possibility to use spray dried granules made from the eutectic mixture of

Table 1
Process parameters of relevant publications regarding powder bed fusion of high performance oxide ceramics.

Publications	Material	Laser	Wavelength [µm]	Laser power [W]	Scanning speed [mm/s]	Spot diameter [µm]	Hatch space [µm]	Layer thickness [µm]	Energy Density [J/mm^3]
Gahler et al. [7] and Heinrich et al. [75]	Al_2O_3 and SiO_2	Cw CO_2 laser	10.6	17–24	35–65	100	40–80	100	26.2–68.6
Wu et al. [8]	Al_2O_3	Cw CO_2 laser	10.6	72	4	2000	N/A	2000	4.5
Deckers et al. [9]	Al_2O_3	Cw CO_2 laser	10.6	2	5.2	400	200	50–200	19.2
Exner et al. [10,71,72] and Regenfuss et al. [11,73]	Al_2O_3 and SiO_2	pulsed Nd:YAG laser (pulse duration: 200 ns or shorter; repetition rate: 0.5–100 kHz)	0.532 or 1.064	N/A	N/A	N/A	N/A	1–10	N/A
Hagedorn and Wilkes [19,20]	Al_2O_3 and Y_2O_3-stabilized ZrO_2 in eutectic ratio	CO_2 laser for preheating and Cw Nd:YAG laser for consolidation	1.064	60	200	200	50	50	30
Florio et al. [22] and Pfeiffer et al. [30,32]	Al_2O_3 doped with Fe_2O_3 and MnO_2	Pulsed Nd:YAG laser (pulse duration: 1.5 ns; repetition rate: 300 kHz)	0.532	5.75	2	135	135	40	532.40
Juste et al. [25]	Al_2O_3 doped with carbon black	Cw fiber laser	1.064	125–150	ca. 109	ca. 30	50	50	332.4–398.9
Ferrage et al. [26]	Y_2O_3-stabilized ZrO_2 with graphite addition	Cw Nd:YAG laser	1.065	84	70	N/A	50	100	240
Mapar et al. [65,66]	Al_2O_3 and Y_2O_3-stabilized ZrO_2 in eutectic ratio	Cw ytterbium fibre laser	1.070	700–900	400	760	400	500	4.6–5.9
Liu et al. [67]	Al2O3/GdAlO3/ZrO2 ternary eutectic ceramic	Cw CO_2 laser	10.6	200	0.1	8	N/A	500	500
Liu et al. [68]	Y_2O_3-stabilized ZrO_2	Nd:YAG laser for preheating and cw ytterbium fiber laser for consolidation	1.060–1.100	30–90	20–5000	34	20	150	1.2–882.3
Liu et al. [69]	Y_2O_3-stabilized ZrO_2	Cw ytterbium fiber laser	1.060–1.100	30–90	10–200	34	80	150	29.4–1764.7
Gan et al. [70]	Al_2O_3 and spodumene	Cw ytterbium fibre laser	1.060–1.100	Up to 400	10,000	80–115	ca. 2	50	7.0–10.0
Zhang et al. [76]	Al_2O_3	Cw ytterbium fiber laser	1.070	200–205	90	60	50	50	759.3
Coulon and Aubry [81]	Al_2O_3	Cw ytterbium fiber laser	1.060–1.100	100	N/A	60	N/A	60	N/A
Liu and Bai [85]	Y_2O_3-stabilized ZrO_2	Pulsed ytterbium fiber laser (pulse duration: 800 fs; repetition rate: 80 MHz)	1.030	131	300	25	20	N/A	N/A
Lee et al [89,90,91]	Al_2O_3, B_2O_3 and Zinc-Borosilicate glass	N/A	N/A	15	560	N/A	125	200–250	0.9–1.1
Bae et al. [92]	Al_2O_3 and glass based on SiO_2–B_2O_3–RO (R = Ba, Zn)	Fiber laser	1.060	20	N/A	50	N/A	1000	N/A
Wang et al. [93,94]	Al_2O_3, ZrO_2 and SiO_2	pulsed Nd:YAG laser (repetition rate: 1400 Hz)	1.064	40	15	100	100	N/A	N/A
Shishkovy et al. [95]	ZrO_2 with aluminum addition	N/A	N/A	50	1500–2000	80	20–40	N/A	N/A
Subramanian et al. [96]	Al_2O_3 with aluminum addition	Pulsed Nd:YAG laser (repetition rate: 20 kHz)	1.060	43	46	N/A	N/A	N/A	N/A
Slocombe and Li [97]	TiO2, Al and C to synthesize TiC–Al2O3	Pulsed Nd:YAG laser (pulse duration: 18 ns; repetition rate: 20 kHz)	N/A	60	2	200–600	100	180	277.8–833.3

Al_2O_3/$GdAlO_3$/ZrO_2 (58/19/23 mol%).

Following the approach of filling voids with smaller particles, Liu et al. [68] showed the possibility also for non-spray dried zirconia powder beds. A coarse powder fraction (22.5–45 µm) and a fine fraction (20 wt% with 9–22.5 µm) were mixed to get the advantages of higher laser light absorptance of the fine powder and better flowability of the coarse fraction. However, when the finer fraction increased, a homogeneous powder deposition was almost impossible due to electrostatic forces. Evaporation of residual moisture was found to increase the flowability in these powders [68,69].

Verga et al. [29] suggested a alternative of carbon distribution within alumina toughened zironia spray dried granules. To achieve a higher

homogeneity the organics in the spray dried granules were pyrolised leaving an amount of carbon of ca. 0.4 wt%. The color of the granules changed from white prior to pyrolysis to black after pyrolysis and tapped powder densities of up to 41 % of the theoretical densities were reached.

In contrary, Ferrage et al. [26] used a simple mechanical blending of micron-sized graphite and YSZ particles. Dense parts could be produced by increasing the powder absorptance from 2% to 57 % with an addition of 0.75 wt% graphite. The flowability of the zirconia powder was not affected by this addition of micron-sized graphite. Furthermore, they applied a roller system to improve the powder packing prior to laser processing. Similarly, Moniz et al. [28] suggested to add nanometric carbon and β-SiC particles to alumina by mechanical blending. They found that the absorption steadily increases with the carbon content and for SiC addition a maximum absorption was reached for 0.5 wt%. Despite this absorption increase, the apparent as well as tapped density and the flowability worsened due to nanoparticles in the final powder blend. Nevertheless, stable parameter windows were found for optimal powder dopant quantities and regular scan tracks could be built. Gan et al. [70] were able to build dense ceramic-glass composites by mechanically blending of 50 Vol% spherical alumina and 50 Vol% irregular shaped spodumene powder. Notwithstanding a poor flowability of the powder (avalange angle of 53.4°), the recoating process ensured a smooth and homogenously distributed powder bed.

B. Mechanical powder bed compaction

Exner et al. [10,71,72] and Regenfuss et al. [11,73] used powder with grain sizes around 1 µm. However, problems with the powder layering in terms of final powder bed density occurred due the nature of the fine particles [10]. They solved this problem depositing the powder with a custom-built machine equipped with a circular coating blade, applying pressure on the powder layer to increase the packing density of the powder bed [72]. Compaction of the powder layer (up to 25 % of TD) took place by elevating the substrate towards a stable lid (maximum compaction pressure 50 kPa) [74]. A higher final part density resulted from a more constant laser light absorption and increased heat conduction [72,74].

C. Slurry casting via doctor blade or rubber scraper

Slurry casting can give powder bed densities up to potentially more than 60 % TD, nanoparticles can be used and the organic content can be minimized [42]. Highly solid loaded, stable slurries with a good fluidity contained for example as solids 25.5 wt% pure α-alumina (d50 = 1.7 µm), 6.0 wt% crystalline silica (d50 = 0.2 µm) and 68.5 wt% amorphous silica (d50 = 11.1 µm) and a water content of 34 wt%, where the particles were dispersed in water by a pH adjustment to 10 [75]. These layers were homogenous and led to dense parts.

Zhang et al. [76] applied a similar approach in terms of a layerwise deposition of an alumina slurry. The ceramic slurry consisted of 50 wt% water and 50 wt% alumina particles with a mean size of 0.62 µm. A rubber scraper was used to apply the dispersion on a preheated alumina substrate (110 °C), which ensured total evaporation of the water.

D. Application via spraying techniques

Another approach to increase the density of the green compact was the deposition of highly solid loaded slurries of dispersed alumina and zirconia by airbrush spraying technique to achieve dense and homogenous layers [77]. However, by application of too much slurry, disconnected planes and rough surfaces were achieved. Furthermore, insufficient wetting and the drying process by an infrared heater led to delamination during processing, which gave porous laser processed parts with a high roughness [77].

On the other hand, aerosol assisted spraying technique gave uniform smooth powder beds with a controllable microstructure and this resulted in complete fusion after laser processing [8]. An ethanol-based alumina (d50 of 0.45 µm) suspension (solid load 5 wt%) was deposited at temperatures close to or over the boiling point by creating droplets with an electrostatic atomizer. Addition of 0.2 wt% polyacrylic acid ensured a stable and homogeneous dispersion by electrosteric stabilization and ensured the lowest viscosity, since excessive dispersant chains can introduce a bridging effect between neighboring particles [8].

Fig. 5. Pure PBF-LB processed alumina parts manufactured by Juste et al. [25].

Fig. 6. Complex structure made from iron oxide doped aluminum oxide powders by a nano-second pulsed green Nd-YAG laser.

E. Electrophoretic deposition

Deckers et al. [9] deposited fine-grained alumina (d50 of 0.3 µm) by electrophoretic deposition (EPD). By friction, the EPD deposited powder layer was transferred from the deposition electrode onto the previous layers. The density of such layers was approximately 57 % of the theoretical density.

3.1.2. Processing methods

The following classification was drawn to classify the different approaches to consolidate powder beds to dense high performance oxides via PBF-LB. This section gives an overview of the approaches to improve properties by increase of absorptance, reduction of melting temperature, reduction of thermal stresses and crack formation and liquid phase formation. Subchapters are as following:

A Use of different dopants
B Use of eutectic material ratios
C Application of preheating
D Application of different lasers and scanning strategies
E Generation of ceramic-glass composites
F Addition of metals to the starting powders
G Combination of PBF-LB with self-propagating high temperature synthesis

The laser parameters used for the different works are summarized in Table 1 at the end of this chapter.

A. Use of different dopants

Juste et al. [25] used 0.1 vol% graphite containing alumina granules to reach a maximum part density of 97.5 % by increasing the powder absorptance of the laser light (Fig. 5). Scanning Electron Microscopy

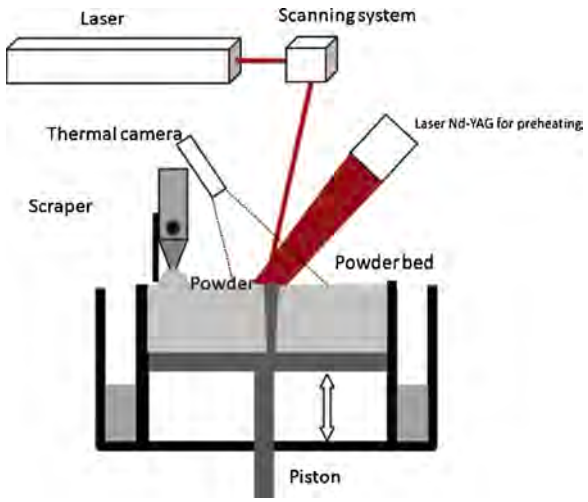

Fig. 7. Schematic of laser preheating with second laser in PBF-LB in accordance to Liu et al. [68].

(SEM) revealed cracks and pores. Pfeiffer et al. [30,32] and Florio et al. [22] showed that iron oxide and manganese oxide can be also effective dopants. However, all dopants did not show significantly reduction of cracks, balling and delamination. Fig. 6 shows complex structures made from iron oxide doped aluminum oxide powders by nano-second pulsed green Nd-YAG laser. Powder diffraction studies on crushed samples confirmed the presence of ternary phases after PBF-LB for both dopants [32], which could be removed in the case of Fe_2O_3 doping by thermal post-treatment. By incorporation of iron atoms into the alumina lattice the ternary phase (hercynite), which is created after the laser melting and resolidifcation, disappeared [63].

Verga et al. [29] and Ferrage [26] showed the possibility to use carbon doping for alumina toughened zirconia (ATZ) and yttria stabilized zirconia (YSZ) to increase the absorptance of the powder. The zirconia was stabilized in both works with yttria to prevent the component to crack because of stresses generated by the strong expansion of the phase transition to monoclinic phase during cool-down. Upon laser processing with a continuous wave Nd-YAG fiber laser ATZ parts with a density of up to 96 % [29] and YSZ parts with a density up to 96.5 % [26] were produced. An overview of the different dopants and material used can be found in Table 1.

B. Use of eutectic material ratios

The use of a eutectic ratio offers the possibility to reduce the melting temperature of the system such as for a mixture of Al_2O_3 and ZrO_2 down to 1860 °C. This mixture should be slightly beneficial to avoid crack formation due to a reduced resolidification temperature and by the toughening of a second phase. Furthermore the bandgap of ZrO_2 (5.8 eV) is slightly smaller than the bandgap of Al_2O_3 (8.8 eV) [78]. Mapar et al. [65,66] produced parts with a continuous ytterbium fiber laser made from Al_2O_3 and YSZ. By the use of high laser powers and low scanning speed ceramic components could be manufactured. However, the parts offered a low density and were fragile and unstable. Zhao et al. [79] observed an oxygen reduction in this powder mixture during laser processing in argon atmosphere, which led to a color change from white to black. This was confirmed by peak shifts in x-ray diffraction pattern. However, they also dealt with inhomogeneous leveling, delamination, balling and cracking effects.

Liu et al. [67] proofed the feasibility to produce ternary eutectic ceramics by laser melting. One powder layer composed of Al_2O_3/G-dAlO_3/ZrO_2 was processed with a CO_2 laser under argon atmosphere to give a ceramic with a density of ca. 98 %. Despite the big laser spot size and low scanning speed, which should be beneficial to reduce thermal stresses, micro-cracks were formed and hardness and fracture toughness were lower than compared with traditional manufactured components [80]. Furthermore, the melting efficacy differed from the center to edge of the laser spot.

C. Application of preheating

To achieve crack free parts, different laser strategies and preheating were applied. In theory, cracks due to thermal stresses are reduced by increasing the ambient temperature during processing and afterwards by controlling the cooling stage. Hagedorn and Wilkes [19,20] processed the eutectic ratio of micron-sized Al_2O_3 and YSZ powder by a dual laser system. Powder consolidation was achieved by a continuous wave Nd:YAG laser and preheating by a CO_2 laser equipped with a diffractive optical element for homogenizing the power output and to deliver temperatures close to the melting point. They found that a preheating temperature of at least 1600 °C was necessary to avoid crack formation. Although the processed parts were almost 100 % dense and without cracks for small parts, they offered a poor surface quality and the size was limited to about 2 mm to avoid cracks.

Liu et al. [68] applied a similar preheating approach to sinter YSZ parts with densities of up to 91 %. Without preheating, they only achieved a density of up to 88 % for parts manufactured [69]. A relatively fast preheating was achieved with a high power Nd:YAG laser (heating within 17−27 s) and powder consolidation was done in a perpendicular scanning strategy by a second laser (Fig. 7). Even though different preheating temperature were tested between 1500 °C and 2500 °C, it was not totally possible to avoid cracks [68]. An additional post-heat treatment of the non-preheated samples showed no effect on the densificationty [69].

Buls et al. [18] used microwaves to generate preheating temperatures of 1100 °C in aluminum oxide powder for processing of single tracks and layers with high densities and without any thermal cracks. For interaction with the microwave energy of 2.45 GHz at room temperature a SiC susceptor was used, since alumina is not absorbing at this wavelength at room temperature. The temperature of the powder was raised by heat conduction and results in lowering of the required laser power for consolidation. However, the use of microwaves can also trigger a thermal runaway at the melt-pool (uncontrolled energy release that further increases temperature during processing), since the absorption of the microwave energy changes for ceramics at higher temperatures.

Coulon and Aubry [81] developed a laser manufacturing process in closed oven that can heat up the powder up to 800 °C. Alumina parts with a maximum densiy of 65 %, a maximum size of 50 mm (fabrication time 15 h) and a minimum wall thickness of 0.3 mm were manufactured by this process.

Deckers et al. [9] produced alumina parts with 85 % density with an applied furnace preheating temperature of 800 °C (homogeneously heated cylindrical zone), that reduced the necessary energy density of the used CO_2 laser required for fusion. Additionally to preheating, a post heat treatment at 1600 °C was performed. SEM of these parts revealed a partial melting, but cracking was not avoided.

D. Application of different lasers and scanning strategies

Different lasers have been already tested to improve the properties of PBF-LB produced high performance oxide ceramics.

In general unmodified high performance oxide ceramics show an absorption of a CO_2 laser light in comparison to Nd:YAG lasers, e.g. alumina powder bed had 96 % of absorption to CO_2 wavelength in [82]. Wilkes and Wissenbach [83,84] used a CO_2 laser mode to manufacture three-dimensional zirconia components. Furthermore, they confirmed a possible processing by a powder bed based direct laser melting of magnesium spinel ($MgAl_2O_4$) and pure aluminum oxide with a CO_2 laser. The final resolution with the CO_2 laser was down to 60 µm and the surface roughness down to 12 µm [83]. In comparison, the use of a Nd:YAG laser led to overheating due to the high intensities necessary to start the absorption process (avalanche effect). The ZrO_2 ceramics showed a dark color after laser processing due to reduction of ZrO_2 and even dark spots on the surface appeared after appropriate heat treatment in air, which were attributed to result from impurities in the raw powders.

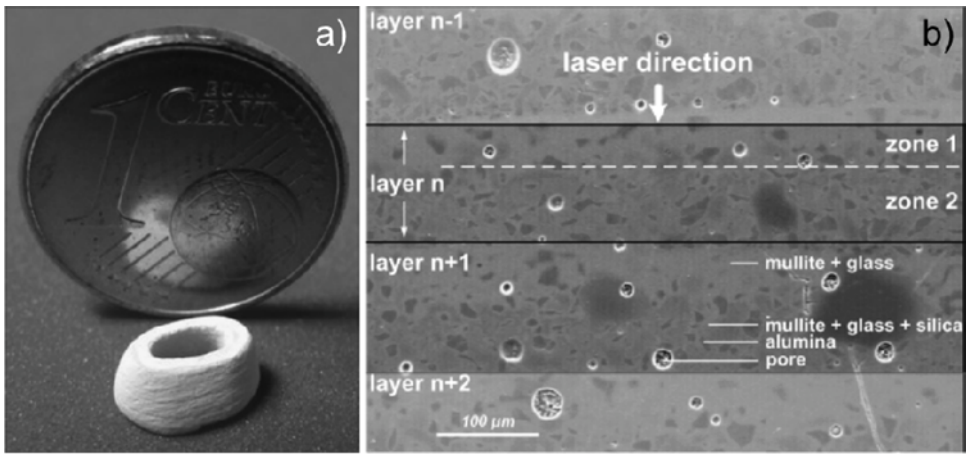

Fig. 8. a) Tooth model consisting of 35 layers (Al2O3–SiO2 ratio: 0.37) and b) typical microstructure of these composite shown in Gahler et al. [7].

In Wu et al. [8] laser processing with a CO_2 laser (energy density of 8.5 J/mm^2) resulted in a complete densification with very few pores in the triple grain boundary. However, the significantly larger laser beam (2 mm) diverges considerably from typical PBF-LB processes, which aim at building small features and achieving accuracy in the order of 0.1 mm.

Zhang et al. [76] optimized the energy density (889–911 J/mm^3) to improve the surface quality of alumina parts. However, rough surfaces as well as cracks were still present. These came mainly from insufficient overlap of the scan tracks, an unstable melt pool, a thermocapillary convection or an exaggerated energy input.

Florio et al. showed the possibility to use a green nanosecond pulsed laser for enhancing the laser-powder interaction in combination with a Fe_2O_3 dopant that has a peak of absorptance at the same wavelength [22]. The use of a slow laser speed and a porous substrate led to smaller thermal gradients and finally to dense and mechanically stable parts, but cracks could not be avoided.

The use of a femtosecond laser for LAM of YSZ was proposed by Liu and Bai [13]. Furthermore, they presented a single step LAM process to produce a fully functional multi-layered solid oxide fuel cell composed of YSZ (electrolyte), Ni-YSZ (anode) and lanthanum strontium manganite (cathode) [85]. For this application, LAM removes the time-intensive, costly and error-prone debinding and sintering and allows to build more complex shapes than only planar or tubular ones, which are typical for conventional methods [85]. In addition, the porosity of the anode can be controlled by the used laser parameters. A 99.5 % dense electrolyte layer (YSZ) was manufactured by using powder with specific surface area of 4.5 m^2/g [13].

E. Generation of ceramic-glass composites

Crack-free selective laser melting of pure silica glass was already shown in literature for single tracks and single layers [86] and also for bioactive glasses [87]. Since pure silica and other glasses have low thermal expansion coefficient and a low glass-transition temperature, they are a promising candidate for LAM. Furthermore, a liquid phase during processing is generated and fuse the powders in short interaction time during the process. However, as described in [7] only rearrangement occurs, and not the other stages like solution precipitation and solid-state sintering typical in traditional liquid phase sintering.

Exner et al. [10,71,72] and Regenfuss et al. [11,73] achieved highly dense parts made of an alumina-silica composite (density up to 98 %) with a resolution of up to 40 µm and an average surface roughness of circa 5 µm by using a pulsed Nd:YAG laser. Manufacturing of parts with aspect ratios of 2 and a maximum height of 10 mm was possible. The created glass phase acted as matrix phase for the crystalline fillers [11]. First tests showed a decomposition of the silica phase due to overheating and thus evaporation [72], similarly to the loss of Si and O from the glass phase described in [88]. A lower intensity of the pulses caused a higher resolution in the parts and less material decomposition. A shrinkage of 0.7 % due to crack annealing (1600 °C) and due to decrease of the pore number was measured [72,73], which led to final mechanical strength of 120 MPa in a 4-point bending test. XRD measurements showed low content of mullite after laser processing, which increased after thermal treatment.

By the use of a nanosecond laser operating with stochastic pulse distribution, it is possible to build parts with relative low stresses and to avoid an overheating due to short times of energy transfer (10−100 ns) and temperature-dependent absorption [11,73]. The stochastic distribution of pulses enabled the consolidation of micro-surfaces which do not overlap at an initial stage and cross-link only towards the end of every layer. A high resolution and the stress-free fabrication results from this selective consolidation [10].The higher photon energy of the green laser leads, according to [10,11,71–73], to higher laser light absorption. In addition, the nanosecond pulses allow to process materials with a bandgap bigger than photon energies, since electrons in the valence band can be also excited due non-linear multi-photon absorption or excited state absorption [11,73]. However, the use of too high intensities involves the risk of overheating (avalanche effect) [11].

The sintering model for the 200 ns pulse irradiation is described in [10,11,71–73] by evaporation and condensation during laser processing. The model contained 4 steps: a) formation of a gas bubble above the molten material, b) rapid bursting, c) formation of a slower jet, and d) dispersion of the jet into droplets and solidfication.

Already in the 90 s, Lee et al. [89–91] tried to implement alumina-glass composites made from aluminum oxide, boron oxide and zinc borosilicate glass powders by PBF-LB. The advantage of the chosen borosilicate glass was the low softening point of only 630 °C. However, additively manufactured parts needed to be infiltrated with silica and thermally post-treated to achieve higher densities and strength values [89].

Bae et al. [92] reported for Al_2O_3 mixed with a grinded glass powder based on a SiO_2–B_2O_3–RO (R = Ba, Zn) ternary system similar results. A black pigment (up to 3 wt%) was added to increase the laser light absorption. A heat-treatment at 750 °C was necessary to achieve high densities (up to 95.3 %) after laser processing (glass softening point of 671 °C). No secondary phase formation by reactions between the amorphous glass and crystalline alumina was observed during the whole process chain.

Heinrich et al. [75], Mühler et al. [6] and Gahler et al. [7] manufactured ceramic parts with densities of up to 92 % of the theoretical density with a continuous wave CO_2 laser light using Al_2O_3 and SiO_2 (Fig. 8). An alumina content smaller than 31 wt% could deliver stable parts. A larger amount of alumina resulted in cracks and delamination

Table 2
Process parameters of relevant publications regarding directed energy deposition of high performance oxide ceramics.

Publications	Material	Laser	Wavelength [µm]	Laser power [W]	Scanning speed [mm/min]	Spot diameter [mm]	Feeding rate [g/min]	Z-increment [mm]
Niu et al. [14]	Al_2O_3	Cw Nd:YAG laser	1.064	375	300	2	1.70	0.5
Fan et al. [16]	Al_2O_3/YAG/ZrO_2 from Al_2O_3 YSZ and Y_2O_3 powders	Cw Nd:YAG laser	1.064	220	558	N/A	N/A	0.5
Balla et al. [17]	Al_2O_3	Cw Nd:YAG laser	N/A	175	600	1.5	14.00	0.254
Su et al. [98]	Al_2O_3/YAG from Al_2O_3 and Y_2O_3 powders	Cw CO_2 laser	10.6	190–450	6–48	4–10	6.0–18.0	N/A
Thakur and Pappas et al. [99,100]	ZTA	Cw CO_2 laser	10.6	275	700–1000	2.5	2.1–3.85	N/A
Wu et al. [101]	$Al_6Si_2O_{13}$ (Mullite) from Al_2O_3 and SiO_2 powders	Cw Nd:YAG laser	N/A	300	200	2	N/A	0.4–0.45
Niu et al. [102]	Al_2O_3	Cw Nd:YAG laser	N/A	350	300	N/A	1.36	0.22
Niu et al. [102]	Al_2O_3/YAG from Al_2O_3 and Y_2O_3 powders	Cw Nd:YAG laser	N/A	320	350	N/A	1.08 (Al_2O_3) and 0.55 (Y_2O_3)	0.18
Fan et al. [103]	Y_2O_3-stabilized ZrO_2	Cw Nd:YAG laser	1.064	325	355	1	4.50	0.5
Pappas et al. [104,105]	$MgAl_2O_4$ from Al_2O_3 and MgO powders	Cw CO_2 laser	10.6	275	1000–2000	2.5	2.1	0.08
Niu et al. [106]	Al_2O_3 and Y_2O_3-stabilized ZrO_2 in eutectic ratio	Cw Nd:YAG laser	N/A	410	400	N/A	1.22 (Al_2O_3) and 0.87 (ZrO_2)	0.25
Huang et al. [107]	$Al_{l2}TiO_5$ and $Al_6Ti_2O_{13}$ (aluminum titanate) from Al_2O_3 and SiO_2 powders	Cw Nd:YAG laser	1.064	250	300	2	N/A	0.4
Mishra et al. [108]	Al_2O_3	Cw fiber laser	N/A	300	600	2.5	8.00	N/A
Niu et al. [110]	Al_2O_3	Cw Nd:YAG laser	N/A	555	700	N/A	4.00	0.5
Niu et al. [111]	Al_2O_3	Cw Nd:YAG laser	N/A	326	300	2.3	1.38	N/A
Wu et al. [116]	Al_2O_3/YAG from Al_2O_3 and Y_2O_3 powders	Cw Nd:YAG laser	N/A	350	340	N/A	1.65	0.21
Niu et al. [117]	Al_2O_3/YAG from Al_2O_3 and Y_2O_3 powders	N/A	N/A	300–350	350	2	1.65	0.21
Fan et al. [118]	Al_2O_3/YAG from Al_2O_3 and Y_2O_3 powders	Cw Nd:YAG laser	N/A	200	305	1	N/A	N/A
Wu et al [133,135]	Hypo- to hypereutectic ratio of Al_2O_3 and Y_2O_3-stabilized ZrO_2	Cw Nd:YAG laser	1.064	250	300–600	2	N/A	0.4
Yan et al. [134,137,138,146]	Al_2O_3 and Y_2O_3-stabilized ZrO_2 in eutectic ratio	Cw Nd:YAG laser	N/A	360	380	2	1.60 (feeding proportion of 42.5 wt% ZrO_2)	0.22
Yan et al. [139]	Al_2O_3 and Y_2O_3-stabilized ZrO_2 in eutectic ratio	Cw Nd:YAG laser	N/A	420	400	2	1.60 (feeding proportion of 42.5 wt% ZrO_2)	0.22
Hu et al. [140]	ZTA	Cw laser	1.07	400	600	0.4	2	0.51
Wu et al. [141]	Al_2O_3 and Y_2O_3-stabilized ZrO_2 in eutectic ratio doped with SiC particles	Cw Nd:YAG laser	1.064	410	500	N/A	3.2–4.0	0.4–0-5
Yan et al. [142]	Al_2O_3 and Y_2O_3-stabilized ZrO_2 in eutectic ratio doped with C-fibers	Cw Nd:YAG laser	N/A	420	400	2	2.2	0.22
Liu et al. [143]	Al_2O_3 and Y_2O_3-stabilized ZrO_2 in eutectic ratio	Cw CO_2 laser	N/A	400–500	3–6	2.5	8–12	N/A
Hu et al. [144]	Al_2O_3 and Y_2O_3-stabilized ZrO_2	Cw Nd:YAG laser	1.064	350	600	0.4	2	0.5–0-8
Ma et al. [145]	Al_2O_3 and Y_2O_3-stabilized ZrO_2 in eutectic ratio	Cw Nd:YAG laser	N/A	530	400	2	2.09	N/A

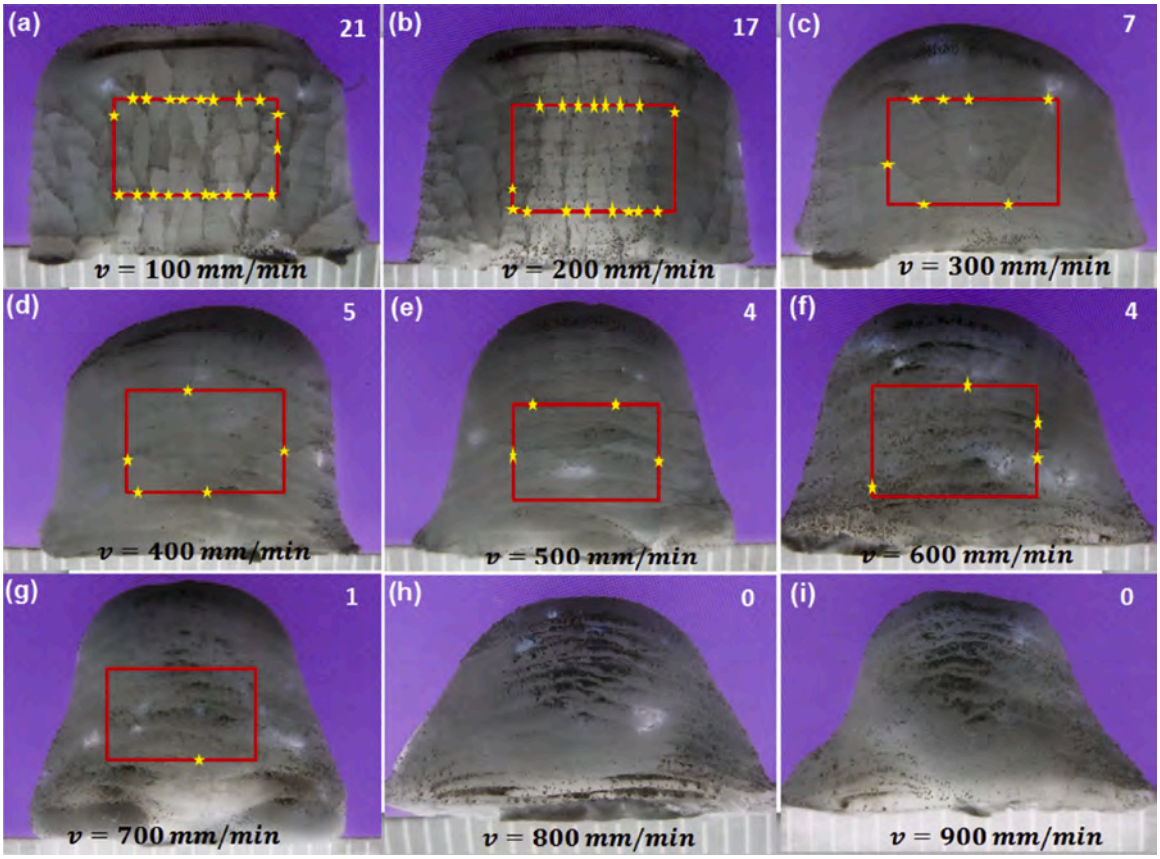

Fig. 9. Crack reduction of Al2O3 single-bead wall structures fabricated by adjusting different processing parameters [110].

issues. An optimized range for the laser energy density to avoid vaporization, decomposition and still fuse the material was evaluated [7] (Table 1). The maximum roughness of the top surface was 4.5 µm. In contrary to the work of Exner et al. [10,71], an increased mullite formation and re-crystallization controlled by dissolution of alumina was reported already after the laser process without thermal post-treatment [75]. A formation of mullite needles is especially interesting due to increase of mechanical stability by reinforcement. An inhomogeneous crystallization within one layer resulted from temperature gradients. A thermal post-treatment further increased the density of the parts to 96 % [75] and led to a formation of cristobalite from the amorphous silica phase and further mullitization [7,75].

Wang et al. [93,94] also used this concept to produce bioceramics made from a alumina-based system containing zirconia and silica by a pulsed Nd:YAG laser (1064 nm). The final product was homogeneous and contained dendrite like-mullite, which is favorable in terms of fracture toughness. The starting YSZ was transformed during laser processing to monoclinic zirconia. By adjusting the alumina-zirconia ratio, the final grain growth of these two particles could be controlled. However, dense parts also contained cracks.

Gan et al. [70] were able to build dense ceramic-glass composites composed of alumina and spodumene with an ytterbium fiber laser in nitrogen atmosphere. Despite of a pre-heating of the substrate, delamination of the part could not be avoided. A layer thickness of 50 µm was identified to achieve the highest density and flexural strength. The microstructure consisted of embedded alumina particles in a partly crystallized glass-ceramic. Despite partial melting of the glass phase, micro cracks were apparent due to difference in the thermal expansion. A heat treatment up to 950 °C led to further crystallization, but was not beneficial for density and mechanical strength in contrast to pure spodumene.

F. Addition of metals to the starting powders

Shishkovy et al. [95] added aluminum to reinforce zirconia to form in-situ homogenous distributed micro-inclusion of Al_2O_3 during PBF-LB. However, the final structures contained pores and cracks and delamination of the part occurred, when the power was too high. In air atmosphere, the free oxygen in the atmosphere promoted formation of alumina. However, destabilization of the tetragonal zirconia phase happened. In argon atmosphere, alumina and intermetallic phases was formed due to decomposition of zirconia.

Subramanian et al. [96] mixed alumina powders with 15, 25 or 35 wt % aluminum to use the metal phase as a binder during manufacturing with a Nd:YAG laser. Laser processing led to a partial oxidation of the aluminum, which could be further oxidized by a post heat treatment. Wetting of the alumina particles with the molten aluminum depended on the achieved temperature (contact angle decrease with temperature). Delamination and cracking were severe, and this limited significantly the mechanical properties.

G. Combination of PBF-LB with self-propagating high temperature synthesis (SHS)

The generation of a high exothermic-reaction (SHS) was another proposal to solve the densification issue in PBF-LB. The used laser energy activated the exothermic reaction of TiO_2, Al and C to synthesize a TiC–Al_2O_3 ceramic. However, the synthesized part showed poor accuracy and high porosity after processing [97].

3.2. Directed energy deposition (DED)

3.2.1. Powder preparation and deposition

Used powders are in general micron sized due to size-driven suppression of agglomeration. However, the use of wet ball mixed nanopowders [98] or mixed submicron and nanopowders [99,100] were also shown to be feasible for processing. Furthermore, a demoisturization process e.g. by a rotary evaporator or a furnace treatment is often done

to ensure good powder flowability of the powder within the nozzles. In case of high hydrophilicity of SiO_2 powder, even if it was micron sized, a special surface modification treatment had to be applied, to avoid blocking of the powder feeding channel and a subsequent stop of the deposition process [101].

The choice of the substrate is essential for processing, since it needs to have a high laser light absorptivity, a good compatibility with the used materials to avoid thermal stresses and ensure a good heat conduction. For example a Ti-6Al-4 V substrate is a good choice for processing of alumina-based materials [102] or yttria stabilized zirconia [103], since it fulfills the described criteria [31]. Other metals or oxides (e.g. alumina [101,104–107]) can be also a chosen. Mishra et al. [108] achieved a higher density and less cracks of alumina parts when fabricated on Ti-6Al-4 V substrates compared to alumina substrates. This was attributed to a more uniform melt pool formation on Ti-6Al-4 V and to the higher thermal conductivity of alumina leading to more cracking during cooling [61,109]. However, Ti was found up to a distance of 2 mm from the substrate in the processed parts by EDS mapping [108]. Furthermore, the substrate can be preheated by multiple time laser pre-scanning [16] or conventional heating.

As a gas to transport the powder through the nozzles usually argon or nitrogen are used. Both gases offers the advantage that gases can escape easy form to melt in contrast to oxygen in air. This reduces porosity and gas inclusions within the part [98]. Furthermore, the inert character of the non-oxidant gases can be helpful to avoid unwanted phase transformation in certain material systems.

3.2.2. *Processing of different materials*

Laser-based DED has been investigated and tested by various authors for different types of high performance oxide ceramics, i.e.:

A Aluminum oxide ceramics
B Zirconium oxide ceramics
C Eutectic ceramic composites
D Zirconia - alumina ceramics
E Alumina/ aluminum titanate ceramics
F Mullite ceramics
G Magnesium aluminate spinel ceramics

The following sub-sections review the state of the art on laser-based DED for all these materials. A summary about the type of the used laser, laser power, powder feeding rate, laser spot diameter, Z-axis increment and scanning speed given by the authors can be found in Table 2.

A. Aluminum oxide ceramics

Balla et al. [17] used DED to produce dense α-Al_2O_3 components with sizes up to 25 mm using a continuous wave Nd:YAG laser. Parts up to 98 % density were produced after heat treatment at 1600 °C. Niu et al. [110] found an optimized processing window by increasing the scanning speed, powder feeding rate and laser power to avoid cracks generated by thermal stresses (Fig. 9). The used energy was also smaller in this case, that results in general in less thermal stresses and the higher deposition rates generated a finer microstructure beneficial for the strength. Mishra et al. [108] found that changing the scanning angle from 0 °C to 67° can increase the final part density (up to 95 %) and reduce the crack formation by a more uniform melt formation. The processed part consisted mainly of α-Al_2O_3 but had also a minor fraction of θ-Al_2O_3.

A mathematical model derived from the energy balance of one deposited layer was used to improve process accuracy by predicting the required laser power at certain process conditions [111]. The process conditions considered were powder feeding rate, scanning speed, spot size and physical properties of the material. For the calculation, material properties were considered constant. The energy required for remelting a part of the previous layer was considered in the calculation. Conduction, convection and radiation were also taken into account. An experimental series showed that the most accurate match of the designed (4 mm) and real (3.96 mm) part width was achieved in experimental trials

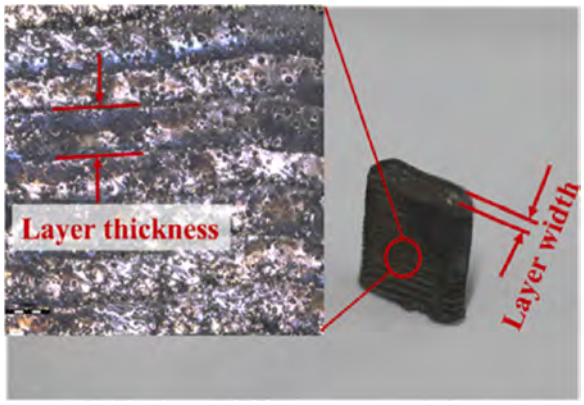

Fig. 10. Thin wall structure with marked layer thickness and width made from YSZ by Fan et al. [103].

with Al_2O_3 by the use of the calculated laser power of 326 W using the set parameters given in Table 2. This was confirmed also for other set parameters. Higher and lower laser powers led to shape distortion, balling and consolidation problems of the parts. Using this model for a suitable laser power prediction of the used Nd:YAG laser, thin walled structures (15 × 4 × 10 mm) and cylindrical structures up to 200 mm in height were produced with densities (evaluated by grey-scale image analysis) up to 99.5 % to study the microstructure and macro properties [14].

Li et al. [112] optimized laser-processing parameters by fabricating single-layers of Al_2O_3 in terms of surface roughness and accuracy. The influence of laser power, powder feeding rate and scanning speed on these layers were evaluated by fixing always two parameters for each study. Bulk parts were also successfully produced; however, the final laser processing parameters were not reported.

B. Zirconium oxide ceramics

Fan et al. [103] fabricated YSZ thin wall structures with a relative density of 98.7 % (Fig. 10). Furthermore, this laser power and the other process parameters described in Table 2 led to the lowest surface roughness and the lowest crack density. However, the decrease of surface tension and viscosity increased the average layer width (2.55 mm–3.33 mm) of the samples. During laser processing the residual monoclinic ZrO_2 phase in the raw powder was transformed into cubic and tetragonal phase. Furthermore, the ZrO_2 parts partly reduced and the created oxygen vacancies led to a dark brown color [113] similar to Verga et al. [29]. Heat treatment at 1000 °C led to the original powder color due to re-oxidation.

C. Eutectic ceramic composites

By the in-situ generation of eutectic ceramic matrix composites, which show a refined interpenetrating microstructure, the mechanical properties in terms of fracture toughness or strength can be improved especially at high temperatures [114,115]. DED offers a great chance to form such materials due to complete melt and fast cooling rates that maintain a small eutectic spacing in the nanometer-range. Due to strict stoichiometric ratio usually no solution or diffusion between involved phases occurs in these composites [114].

Wu et al. [116] produced Al_2O_3-YAG eutectic ceramics from Al_2O_3 and Y_2O_3 powders (81.5/18.5 mol%) with a continuous wave Nd:YAG laser. A water cooling of the substrate increased the cooling rate 300 times. This changed the microstructure to a dendritic structure and reduced the eutectic spacing by 78.1 % due to a higher undercooling and solidification rate. This in terms increased also microhardness and fracture toughness. Furthermore, the eutectic phase composition was not affected by the cooling. Similarly, Niu et al. [117] produced Al_2O_3-YAG ceramics with 98.6 % density by DED. The absence of cooling led to a higher melt pool temperature and thus to a bigger melt-pool at the end of the scanned path, which gave in consequence a

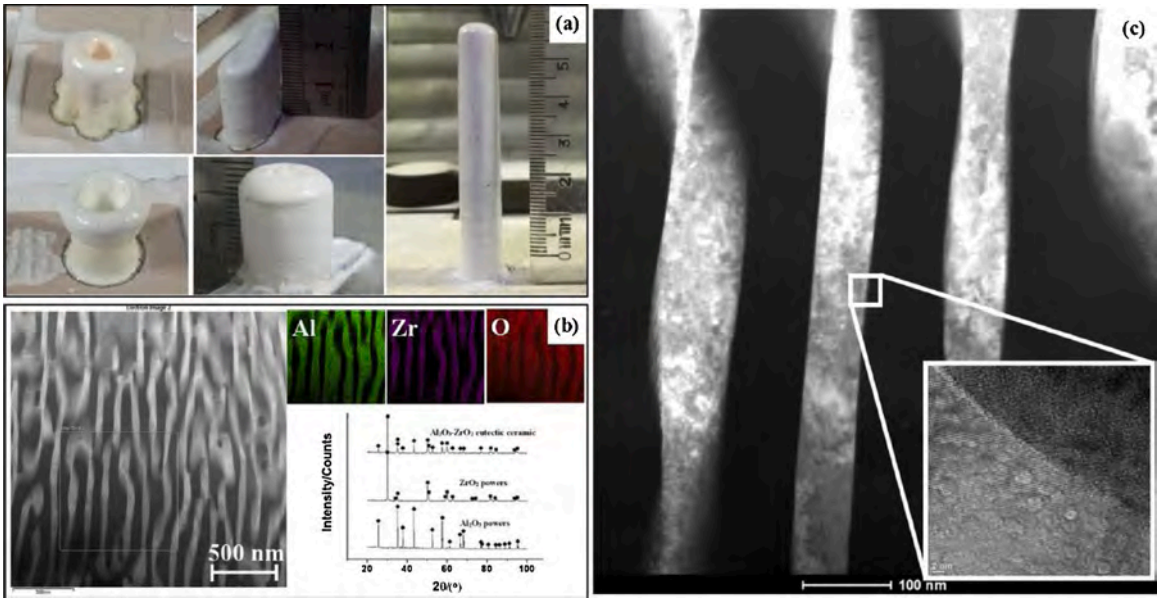

Fig. 11. a) Various Al_2O_3-ZrO_2 eutectic ceramic samples, (b) SEM micro-structure, element distribution and XRD phase diagram, (c) TEM micro-structure and phase boundary [139].

dumbbell shape structure.

Su et al. [98] and Fan et al. [118] gave different models to describe the special microstructure formation of the eutectic Al_2O_3-YAG ceramic. Su et al. [98] focused hereby on the irregular growth and transition mechanisms. Furthermore, by the use of preheating with a CO_2 laser up to 1300 °C, they showed the possibility to reduce crack formation. According to described solidification behavior, a physical model based on atom cluster was proposed, in which first YAG clusters were formed before Al_2O_3 clusters. By remaining a strict interface separation, a mixing at the phase interfaces occurred subsequently. Fan et al. [118] investigated impact of thermal gradient, and thus solidification rate, on the eutectic microstructure in different sample regions. This irregular structure refinement is explained by the Jackson criteria ($\Delta S/R_s > 2$ for irregular growth, where ΔS is the melting entropy and R_s the gas constant), which describes that the high melting entropies lead to a highly anisotropic growth [119,120]. The general growth behavior of the sample (in general dependency of interphase spacing from solidification rate) was accurately described by the Magnin Kurz model [121]. A transition from irregular to regular eutectics usually follows the magnitude of the undercooling.

Fan et al. [16] showed the possibility to fabricate dense (>98 %) ternary eutectic composites (ca. 40 vol% Al_2O_3, 43 vol% YAG, 17 vol% ZrO_2) with refined microstructure made from 54 wt% Al_2O_3, 27 wt% Y_2O_3, 19 wt% ZrO_2 powders (8 wt% Y_2O_3 stabilized) by DED. These composites are from particular interest, since they can possess superior mechanical properties compared to binary Al_2O_3/YAG and Al_2O_3/ZrO_2 eutectics [122–124] and showed superplastic behavior above ca. 1330 °C [125]. The evolution of the eutectic interphase spacing dimensions along build direction match the Jackson-Hunt relation very well [126]. The preference of an irregular morphology within the sample depends on the tendency of the phases to faceted growth. Even if only one phase prefers faceted growth, the whole morphology becomes irregular [127]. The tendency in faceting can be described by the so called Jackson factor α (α < 2: non-faceted; 2 < α < 5: weakly or non-faceted; α > 5: faceted) [128,129]. In this case, Al_2O_3 tends for example to a strong faceted growth, whereas ZrO_2 has a weak tendency to faceted growth [130]. To evaluate the solidification mechanism, a 3D finite volume method model was used to estimate temperature distribution, thermal gradient and solidification rates during processing. Since the cellular growth does not agree with the model, it is concluded that the upper part of each layer is remelted during subsequent layer application.

D. Zirconia - alumina ceramics

Zirconia inclusions are known to increase the poor fracture toughness of alumina ceramics by crack bridging and deflection [131] as seen already for traditional processing routes [132]. A further toughening mechanism can be that a stress induced toughening by volume expansion due to phase transformation from tetragonal ZrO_2 to monoclinic ZrO_2 happens at the crack tip. However, the size of the ZrO_2 is crucial to preserve the t-ZrO_2 phase [133]. Thakur and Pappas et al. [99,100], which could nearly eliminate cracking during DED by doping alumina ceramics with up to 10 wt% zirconia and substrate preheating (450 °C), found marks of this transformation. Overall, the cumulative crack length of 19 cm decreased to 0.15 cm by doping in parts with a length of 60 mm and diameter of 5–6 mm. Furthermore, the yield of powder to final part conversion could be increased to 60 % with optimized process parameters. However, Wu et al. and Yan et al. did not find evidence for this stress induced phase transformation in their works [133,134] and Wu et al. reported that it can also depend on the Al_2O_3/ZrO_2 ratio [135]. Another advantage of zirconia is that it decreases the thermal conductivity in alumina [136] and has an impact on thermal gradient and cooling rate.

Solving the issues of cracking and pore formation is a key issue in DED production. One of the methods to overcome these issues is the application of an external ultrasonic field to change the microstructure to a smaller eutectic spacing with no obvious grain boundaries. This is applicable only to parts up to a certain height. Ultrasonic power provides an increase of melt pool pressure and thus an increase of the free energy change, which in terms decreased the critical nucleus size and the critical nucleation energy [137]. This resulted in samples with lower porosity and crack amount, since crack generation was greatly aggravated by this uniform refined three-dimensional network structure. Furthermore, the lifespan, area and width of the melt pool increased due to more energy absorption and thus gases had more time to escape [138]. Heat accumulation in one layer became larger and thus the thermal gradient smaller [134]. However, too high ultrasonic power led to a reduction of the temperature gradient and in consequence to an increase of the eutectic spacing. This had a contrary effect on the part density, which changed to entirely dense, since the stirring and crushing effect and the lower melt pool viscosity by the ultrasonication helped trapped gases to escape easily [139]. Too low ultrasonic power resulted

Fig. 12. Irregular structures fabricated by directed energy deposition of Al_2O_3 and TiO_2 powders [147].

in inhomogeneous dendritic growth due to an increased growth rate of the ZrO_2 phase [138]. Various suitable specimen shapes with corresponding microstructure analysis are shown in Fig. 11. Hu et al. [140] described similar effects for composites with only 10 wt% zirconia. The parts had better mechanical properties (wear rate, microhardness and compressive strength), ductility and grain refinement (alumina grains down to 8 μm) compared with parts fabricated without ultrasonic vibration. Furthermore, the preferred crack propagation changed from solely inter-crystalline to partly trans-crystalline.

An addition of a third phase can be considered as the second way to solve the porosity and crack problem. Wu et al. [141] effectively added up to 25 wt% SiC particles to overcome this issues. These particles could be uniformly distributed within the samples and the interfaces of the particles were firmly bonded due to ZrC and $ZrSi_2$ formation. The additional absorptance and thus a higher melt pool temperature are other positive effects. Furthermore, the large thermal expansion coefficient mismatch generated large residual stress around the doping particles. Yan et al. [142] reported that addition of 4 wt% carbon fibers further decreased the spacing to 50 nm of an eutectic composite due to an accelerated cooling rate and provision of more nucleation sides, and as well increased the fracture toughness due to grain refinement and whisker toughening [142].

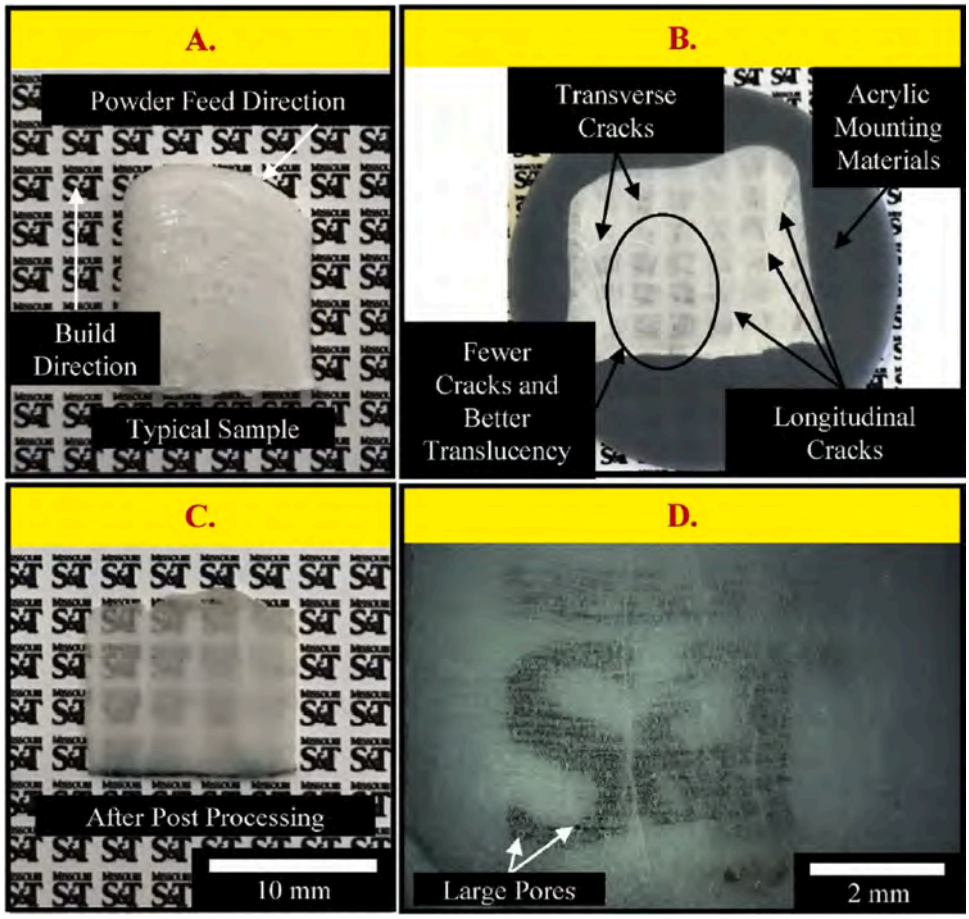

Fig. 13. A) Typical printed thin wall magnesium aluminate spinel ceramic samples. B), C) printed (powder flow rates of 0.8 g/min and 2.1 g/min, respectively) and post-processed samples. D) higher magnification with optical microscope of sample in C) [104].

Table 3
Properties of parts processed by PBF-LB.

Publications	Material	Porosity	Cracks	Geometrical accuracy and surface quality	Microstructure	Mechanical properties (test method)
Gahler et al. [7] and Heinrich et al. [75]	Al_2O_3 and SiO_2	8%	N/A	N/A	Mullite needles	N/A
Wu et al. [8]	Al_2O_3	N/A	N/A	N/A	Relatively fine grains (1.5 μm)	N/A
Deckers et al. [9]	Al_2O_3	15 %	Yes	High porosity and high inhomogeinities	Inhomogeneous, grains of tens of micrometer	N/A
Exner et al. [10,71,72] and Regenfuss et al. [11,73]	Al_2O_3 and SiO_2	2%	No	Not evident defects High surface and geometrical accuracy. $R_a < 5$ μm Resolution of 40 μm	Generation of mullite. Some porosity left even after post-heat treatment.	120 MPa (4-point bending)
Fan et al. [12]	Al_2O_3	N/A	Yes	N/A	Columnar dendrites Equiaxed dendrites for high energy densities	15−20 GPa (Vickers microhardness)
Buls et al. [18]	Al_2O_3, ZrO_2	N/A	No	Not evident in single layer	N/A	N/A
Hagedorn and Wilkes [19,20]	Al_2O_3- ZrO_2 eutectic ratio	< 3 %	No	Poor surface	Fine eutectic structure	> 500 MPa (B3B)
Florio et al. [22] and Pfeiffer et al. [30,32] and	Al_2O_3 Fe_2O_3- and MnO_2-doped	< 5%	Yes	Slight balling	Uniform, except cracks	25.1 MPa (average, B3B)
Juste et al. [25]	Al_2O_3, carbon-doped	2.5 %	Yes	Concave upper surface	Porous and irregular	N/A
Ferrage et al. [26]	Yttria-stabilized ZrO_2	3.5 %	Yes	Not evident defects	Columnar crystals	N/A
Verga et al. [29]	ATZ (Al_2O_3 20% - ZrO_2 80%) Carbon-doped	4%	Yes	Not evident defects	Al_2O_3- ZrO_2 partially eutectic system	31 MPa (4-point bending)
Mapar et al. [65,66]	Al_2O_3- ZrO_2 eutectic ratio	30.6 %	No	High porosity and inhomogeneity	Porous and flake-shaped	N/A
Mapar et al. [65,66]	Al_2O_3- ZrO_2 eutectic ratio	N/A	Yes	Delamination Slight balling	Fine eutectic structure	N/A
Liu et al. [67]	Al_2O_3 /$GdAlO_3$ /ZrO_2	< 2%	No	N/A	"Chinese script", lamellae, rod-like microstructure varying with position	15.3 GPa (microhardness)
Liu et al. [68]	Yttria-stabilized (7%) ZrO_2	9 %	Yes	Poor surface	Homogeneous, except cracks	N/A
Gan et al. [70]	Al_2O_3 (50%) and spodumene (50%)	> 5%	Yes	Delamination at substrate	Composite – alumina included in spodumene matrix	< 12 MPa (3-point bending)
Zhang et al. [76]	Al_2O_3	N/A	Yes	N/A	Columnar crystals	N/A
Coulon and Aubry [81]	Al_2O_3	35 %	N/A	N/A	N/A	15 MPa (tensile test)
Wilkes [83,84]	Mainly ZrO_2 with addition of other unspecified oxides	N/A	Yes	Roughness R_a below 12 μm	Fine and homogeneous grains (below 2 μm)	9.8 MPa (4-point bending)
Liu and Bai [85]	YSZ (7% yttria)	12 %	Yes	Deformations and crack at substrate interface. Unmolten particles on the surface	Tetragonal crystals	18.84 GPa (microhardness)
Lee et al [89,90,91]	Al_2O_3, B_2O_3 and zinc borosilicate glass	N/A	N/A	N/A	Formation of aluminum borate and gahnite.	70−110 MPa after Ceracon forging (4-point bending)
Bae et al. [92]	Al2O3 and glass based on SiO2–B2O3–RO (R = Ba, Zn)	< 5%	No	Not evident defects	No formation of secondary phases. Molten glassmatrix for alumina content < 30 wt%	7.57 GPa (Vickers microhardness)
Wang et al. [93,94]	Al_2O_3, ZrO_2-SiO_2 3 different combinations	N/A	N/A	N/A	Mullite needles Silica-based matrix	N/A
Shishkovy et al. [95]	ZrO_2 (80%) and Al_2O_3 (20%)	N/A	Yes	Large porosities	Intermetallic phases	N/A
Subramanian et al. [96]	Al_2O_3 and Al	65 %	Yes	Delamination	Agglomerations	N/A

The third possibility is to preheat the surface. However, a coarse microstructure can be generated by this. Liu et al. [143] applied an additional pre-heating up to 1000 °C to process crack-free and pore-free eutectic Al_2O_3/ZrO_2 ceramics. The microstructure was a typical columnar colony structure resulting from constitutional undercooling. The inter-colony spacing decreased with increasing scanning rate and the change of the average rod spacing (λ_{av}) inside the colonies on the scanning rate (V) could be described by the relation $\lambda_{av}V^{0.5} = 1\ \mu m^{1.5}\ s^{-0.5}$. The growth of these colonies was described by a model, which proposed a growth normal to the macrofaceted solid/liquid interface accompanied by the nucleation on of ZrO2 on the coarsening edge at the apex of the colony.

Other authors tried additionally to optimize the ZrO_2 amount. Hu et al. [144] studied amounts up to 41.5 wt% (eutectic ratio). High thermal gradients (small spot size of 0.4 mm) generated micro-cracks, especially in pure Al_2O_3. With increased ZrO_2 content the laser light absorption changed and thus part height decreased and part color changed from grey to white. A fully formed eutectic network was first seen at a ZrO_2 content of 10 wt%. Wu et al. [133] studied the influence of ZrO_2 doping by using process parameters that tend to form cracks. The best crack suppression was achieved with the eutectic ratio (crack density reduce: 43.2 %). This eutectic ratio was used by many research gropus [106,145,146].

Niu et al. [102] compared microstructure of Al_2O_3, Al_2O_3/YAG and Al_2O_3/ZrO_2 (both in eutectic ratio). The process parameters for every material were different due to optimization (Table 2). In pure Al_2O_3 parts, microcracks and a few macrocracks appeared. Whereas the crack formation in Al_2O_3/YAG ceramics was already suppressed due to fine-grained microstructure with a eutectic spacing smaller than 1 μm, the cracks were totally suppressed in the nano-structured Al_2O_3/ZrO_2 ceramic.

E. Alumina/ aluminum titanate ceramics

The potential of crack reduction or even total suppression in melt grown ceramics is offered by in in-situ reactions. A possible starting

Table 4
Properties of parts processed by DED.

Publications	Material	Porosity	Cracks	Geometrical accuracy and surface quality	Microstructure	Mechanical properties
Niu et al. [14,110, 111]	Al_2O_3	0.5%	No	Beam size of 2 mm. Only thin-walled and cylindrical structures without cracks	Columnar Grains: about 60 µm width, several hundreds of µm in height	210 MPa (3-point bending) 395 MPa (compression strength)
Fan et al. [16]	Al_2O_3, YAG and Zr_2O_3 (ternary eutectic, 54/ 27/19 wt%)	<2%	Yes (only at bottom and top)	Only thin-wall structures.	Cellular irregular and fine eutectic of 3 phases.	18.9 GPa (Vickers micro-hardness) 3.8 MPa $m^{1/2}$ (indentation-derived fracture toughness)
Balla et al. [17]	Al_2O_3	2 %	No	Beam size of 1.5 mm	Columnar grains: about 5 µm width and 254 µm height	159 MPa/276 MPa (compressive strength, build direction/normal)
Su et al. [98]	Al_2O_3 and Y_2O_3 (binary eutectic ratio, 82/18 wt %)	~0 %	No	Beam size of about 4–10 mm.	45.5 %Al 2 O 3 /54.5 %YAG (eutectic). Fine eutectic structure (<100 nm)	N/A
Thakur and Pappas et al. [99,100]	Al_2O_3 with YSZ doping up to 10 wt%	Ca. 6.5 %	Yes	Beam size of 2.5 mm.	10 wt% YSZ: 18 µm average grain size.	208 MPa (4-point bending)
Wu et al. [101]	Al_2O_3 (71.8 wt%) and SiO_2 (28.2 wt%), mullite stoichiometric ratio	2.2 %	Yes	Beam size of about 2 mm.	Columnar Grains: 16.57 µm width. Cracks in the center of the cross-section, pores towards the edges.	62.8 MPa (3-point bending)
Niu et al. [102]	Al_2O_3 Al_2O_3 and Y_2O_3 (66.5/ 33.5 wt%) Al_2O_3 – YSZ eutectic	N/A	No (only for Al_2O_3 – YSZ)	Beam size of about 2 mm. Cylinder longer than 50 mm. Thin wall, arc-shaped structure	Fine eutectic structures < 1 µm	>14.71 GPa (Vickers microhardness)
Fan et al. [103]	YSZ	1.3 %	Yes	Roughness Ra 20–40 µm. Beam size of 1 mm.	Tetragonal banded ZrO_2 embedded in cubic ZrO_2 matrix	19.5 GPa (nanoindentation)
Pappas et al. [104, 105]	Al_2O_3 and MgO (spinel stoichiometric ratio)	Ca. 2 %	Yes	Beam size of about 2–2.5 mm.	$MgAl_2O_4$ is generated uniformly. Porosity mainly below 30 µm	N/A
Niu et al. [106], Yan et al. [134,137,138, 139,142,146], Ma et al. [145]	Al_2O_3 – YSZ eutectic	0.1 %	Yes	Beam size of about 2 mm. Only cylindrical and thin wall structures.	Fine eutectic microstructure with spacing below 100 nm	18.6 GPa (Vickers microhardness)
Li et al. [112]	Al_2O_3	N/A	N/A	Roughness Ra of 4.6 µm. Flatness of 0.08 mm. Width of a single track around 1.5 mm	N/A	2000 HV0.2 (Vickers microhardness)
Wu et al. [116], Niu et al. [117]	Al_2O_3 and Y_2O_3 (66.5/ 33.5 and 56/44 wt%)	1.4 %	N/A	Beam size of about 2 mm.	Fine eutectic structures < 240 nm (with substrate cooling)	Up to 21.5 GPa (Vickers microhardness, with substrate cooling)
Fan et al. [118]	Al_2O_3 and Y_2O_3 (56/44 wt% eutectic)	N/A	N/A	N/A	Colony structure of irregular and fine eutectic phases.	N/A
Wu et al. [135]	Al_2O_3 with different ratio of YSZ-doping up to 65 wt% of YSZ	N/A	No	Beam size of about 2 mm. Complex structures, but with evident deformations. Cylinders up to 230 mm in height	Similar to Hu 2018 and Hu 2020.	237 MPa (3-point bending)
Hu et al. [140,144]	Al_2O_3 with different ratio of YSZ-doping up to eutectic YSZ (41.5 wt %)	N/A	Yes	Beam size of 0.4 mm	10 wt% YSZ: 8 µm average grain size of Al_2O_3, YSZ at grain boundaries Fine eutecitc structures for eutectic ratio.	Ca.450 MPa (compressive strength)
Liu et al. [143]	Al_2O_3 – YSZ eutectic	N/A	Yes	Beam size of about 2.5 mm.	Columnar colonies distanced by 20–100 µm made of eutectic fine lamellae with spacing below 100 nm.	16.7 GPa (Vickers microhardness)
Wu et al. [148], Niu et al. [147], Huang et al [107]	Al_2O_3 and TiO_2 (up to 44 wt%)	1 %	No	Beam size of about 2 mm. Crack-free irregular parts up to 30 mm of wall thickness and 150 mm of length	$Al_6Ti_2O_{13}$ matrix, alumina grains. Fine lamellae eutectic structure of Al_2TiO_5 and $Al_6Ti_2O_{13}$ for high content of TiO_2	212 MPa (3-point bending)
Li et al. [156,157]	Al_2O_3 with different ratio of YSZ-doping up to 65 wt% of YSZ	N/A	Yes	Beam size of about 2.5 mm.	Fine eutectic structure acts as matrix around dendrites for non-eutectic ratios.	21.4 GPa (Vickers microhardness)

combination can be for example alumina and titania powders to form aluminum titanate during DED [107,147,148]. This phase has a low thermal expansion coefficient, low thermal conductivity and therefore excellent thermal shock behavior [149] and improves the fracture toughness of Al_2O_3 through crack deflection and residual compressive stress regions [150,151]. Crack-free parts up to 30 mm in width and up to 150 mm in height made of alumina and aluminum titanate ($Al_2TiO_5/Al_6Ti_2O_{13}$) could be manufactured by DED using powder containing over 30 wt% of titania (Fig. 12) [147]. For a lower amount of titania, cracks were still occurring.

F. Mullite ceramic

DED offers also the chance to create mullite made from a stoichiometric ratio of (crystalline) alumina (71.8 wt%) and (partly crystalline) silica (28.2 wt%) [101]. This allows also gaining a better understanding of mullite crystal growth from the melt. Mullite has a low thermal expansion coefficient, which is beneficial for reducing thermal stresses. A continuous wave Nd:YAG laser was used to produce cylindrical samples with a height of up to 34 mm, a diameter of 5–6 mm and a density

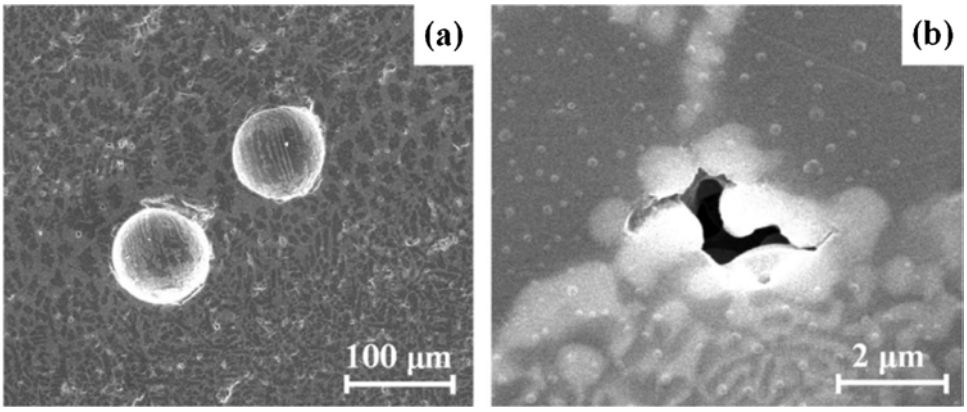

Fig. 14. a) spherical porosity due to entrapped gases. b) irregular porosity generated during shrinkage because of insufficient enegery input [134].

of 97.8 %. Even though the density was higher than in traditional formed mullite ceramics [152], the mechanical properties were lower due to defects [153,154] such as pores and cracks within the microstructure. The growth speed in z-direction was 350 mm/h, which is high compared to the growth speed of traditional methods (e.g. 100 mm/h for laser floating zone technique [155]).

G. Magnesium aluminate spinel ceramics

Pappas et al. [104,105] showed the possibility to directly fabricate translucent magnesium aluminate spinel from a homogeneous blend of alumina and magnesia, which were shown to maintain the stoichiometric ratio during laser processing. Both starting powders were micron-sized, which offers a great chance of cost reduction by this way of production, since nanosized spinel powders have to be used in traditional sintering [104]. However, the produced samples by DED had to be also mechanically post-processed due to high surface roughness and residual cracks and pores, which scatter strongly the incident light (Fig. 13). The highest transmittance after polishing measured by an integrating sphere was 46 % [104]. In the top regions of the sample large shrinkage cavities were observed due to insufficient liquid phase replenishment during solidification. An increase in laser power led to a reduction of the size and amount of pores, but also to a severe decrease of print resolution.

4. Properties of laser additive manufactured parts and open challenges

There are still several open challenges for LAM of high performance oxide ceramics, because several defects typical of LAM techniques affect the properties of the produced parts. In this chapter, the most relevant defects are reviewed and their effects on properties is thoroughly discussed, focusing on the physical causes and the solutions to the open challenges. The mostly affected properties could be categorized as follows:

- **Porosity** due to poor densification
- **Microstructural properties** involving grain size, grain boundaries and phase transformation.
- **Mechanical properties** affected by e.g. thermal-induced cracks and microstructure.
- **Geometrical accuracy and surface quality defects** due to instabilities and/or residual stresses.

Tables 3 and 4 show a summary of the properties of all the reported works.

4.1. Porosity

High part density, and therefore low porosity, is a necessary requirement for high performance ceramics in engineering applications with high mechanical requirements. In fact, the mechanical strength of ceramics typically decay exponentially with an increase of porosity according to the empirical law of Duckworth [158]. LAM processes often lead to poor densification of the starting powder depending on process conditions and thermophysical properties of the material. For these reasons, density measurements are generally performed and reported in most publications about AM of ceramics.

The most common measurements of porosity are derived from Archimedes density measurements or density measurements based on the geometrical dimension and weight of the part. Challenges of these methods are, that Archimedes measurements cannot take into account the open porosity, which can be relevant in case of small and porous parts, whereas on the other side measuring the size and the weight is often linked to large measurement errors in the dimensions.

A modified version of Archimedes test is described in the standard ASTM C20-00 (2015) [159] applied by Verga et al. [29]. This version takes into account the open porosity of the sample. The parts are measured not only dry and under water, but also wet, so that the volume of water filling the open porosity can be estimated. However, the size of the measured sample, according to the standard, should be a cube of 50 mm quartered from a larger specimen, while generally smaller samples are built in LAM.

Another measurement possibility for porosity consists in analyzing a cross-section of a sample after grinding and polishing. Liu and Bai [85] used this method for the measurement of the density of a single layer and Liu et al. [68] used it even for entire parts. However, this method is extremely time consuming and provide information of only a single cross-section. Furthermore, the sample is destroyed by the preparation of the cross-section.

Finally, computer tomography (CT) allows to have a full 3D model, from which calculations of porosity can be accurately performed, as long as the size of the sample is small enough to allow x-ray penetration. Pfeiffer et al. [32], Mishra et al. [108] and Gan et al. [70] used it to analyse 2 mm cubes and 3 × 4 mm pillar. Gan et al. compared the Archimedes method with CT scan measurements: the density calculated was ca. 88 % according to Archimedes principle and ca. 95 % according to micro-CT for the same part [70]. The difference was probably due to the unknown theoretical density of the LAM produced material. A clear advantage of computer tomography is also the possibility to analyse at the same time other defects, such as cracks as well as geometrical and surface defects, when the resolution is high enough.

Considering the variety of used measurement methods and the large deviation in the measurement results, it is difficult to compare results from different publications. However, for PBF-LB it can be noticed that values of porosity lower than 10 % for high performance ceramics, such as alumina, zirconia or a combination of the two, could be achieved only by using high temperature preheating (above 1600 °C) [19,20,68] or by

using powder doping with other colored oxides [22,30,32], or with graphite [25,26,29]. This proves that poor laser light absorption at room temperature is the leading cause for high porosity in PBF-LB. Other proven causes for high porosity are irregular powder shape [20], insufficient laser energy density [13,22], low laser pulse repetition rate [22] and a too large layer thickness [23,25,70].

Furthermore, Exner et al. [10,71,72,74], Regenfuss et al. [11,73], Gahler et al. [7] and Heinrich et al. [75] could also achieve porosity lower than 10 % by using composite materials including silica and alumina and a CO_2 laser, or by using spodumene and alumina in equal ratio as starting material [70].

In DED achieving high density is less critical. Several authors recorded densities around or above 99 %, such as [14] for alumina and [103] for YSZ without any additive. This could be explained by the fact that power and spot size in DED are generally one order of magnitude larger than in PBF, which may lead to a different temperature distribution.

Yan et al. distinguished between porosity generated by entrapped gases, which is generally spherical or ellipsoidal, and irregular porosity due to the rapid shrinkage from melt to solid [139]. Fig. 14 shows an example of both types of porosities. Wu et al. [101] and Niu et al. [14] showed that pores in DED parts made of mullite and alumina are predominantly located at the boundaries due to the higher viscosity of the melt pool in this region, which remains colder compared to the center. Li et al., instead, noticed irregular porosity due to fast shrinkage in the center of the alumina-zirconia samples [156,157]. The authors also showed that the right choice of processing parameters and the addition of ultrasonic vibrations reduces drastically both types of porosity.

Liu et al. recorded that porosity due to fast shrinkage could be avoided with a sufficiently high energy density, specifically with a slow scanning rate (smaller than 0.1 mm/s) and a high power (above 400 W) [143]. Similarly, Pappas et al. [105] verified that an optimal speed for porosity reduction exists for producing the spinel $MgAl_2O_4$ starting from MgO and alumina powder. Porosity could be reduced with a smaller layer thickness and smaller spot size, which means increasing volumetric energy density.

According to Pappas et al. [105], nano-sized MgO (<50 nm), filling the voids between the coarser powder, improved flowability and packing density of the powder mix compared to micron-sized MgO (< 44 μm), which was beneficial for reducing entrapped gas porosity. The influence of a pulsed laser (0.24-10 ms) did not have an impact in comparison to a continuous laser with the same power.

As can be understood from the comparison of Tables 3 and 4, porosity in PBF-LB is more critical than in DED and it can be solved only by using specific materials and process combinations. In DED high densities could be achieved through process parameter studies with several materials and different lasers. Porosity generated by the entrapped gases are typical for DED. It is due to the large melt-pool typical of this process and to the presence of a large gas flow directed into the melt-pool, which is necessary to carry the powder. However, this porosity could be minimized through process parameter studies and the addition of ultrasonic vibrations.

4.2. Microstructure

Typically for LAM techniques, part shape and microstructure are generated simultaneously during the melting and resolidification process. This means that tailoring the microstructure, such as grain size and shape, is challenging, since the microstructure obtained is heavily dependent on the processing conditions and often only small parameter windows are available. Especially, the microstructure has hereby a large impact on mechanical or other desired physical properties.

In the case of PBF-LB of pure alumina, the low speed and high power, required to have dense parts and to reduce cracks, lead to large grains. Deckers et al. [9] could achieve grains diameters as low as 5 μm by PBF-LB, but density was limited to 85 %. Zhang et al. [76] and Zheng et al. [15] noticed that lamellae structures of few microns in width and tens of microns in length were generated along the build direction by thermal capillary convection, influenced by Marangoni effect, streak convection and flowing Bénard cells. Ferrage et al. [26] measured columnar grains of 50 ± 8 μm in width (parallel to the building direction) and 10 ± 2 μm in thickness using YSZ and observed some pores with a mean size of 1 μm. Fan et al. [12] observed that columnar dendrites transformed into equiaxed dendrite at high energy densities. In addition, they found a correlation between energy density and grain size: higher energy density imply also lower cooling rate and therefore larger grains. Pfeiffer et al. [30,32], Florio et al. [22] and Makowska et al. [63] did not provide data on grain sizes, but large grains of at least tens of microns could be assumed from the narrow and high XRD peaks. Wu et al. [8] achieved small spherical grains of about 1.5 μm using a large beam (2 mm), because of liquid phase sintering with small amounts of impurities. However, the study was limited to a single layer. In [160] using a CO_2 laser and without preheating, small grains with sizes between 500 nm and 2 μm were formed, which were much smaller than the original powder particles. This was explained by the rapid cooling provided by the fast moving of the scanning laser.

The situation is quite different for eutectic compositions or other composites. Mapar [66] observed for eutectic alumina-zirconia flake--shaped microstructure. This was explained by the difference in surface tension between the two materials. Finer grains were obtained using a laser with a small spot size (80 μm, instead of 760 μm) and higher scan speed (250 mm/s). This was explained by the higher cooling rate induced by the smaller spot and faster speed. Verga et al. [29] observed crystalline zirconia surrounded by alumina, which is supposedly amorphous before a post heat treatment. Liu et al. [67] used a ternary eutectic starting material and obtained different eutectic structures at different position in the samples. At the bottom, ultra-fine colony microstructures are evident, at the top rod-like eutectic structures are dominant and lamellae structures are seen in between. The interphase spacing of the eutectic is also varying from 0.92 μm at the bottom to 0.48 μm at the top.

Using a second laser for high temperature preheating, Hagedorn et al. [19] obtained a nano-sized microstructure interrupted by coarser crystals in intervals of 50 μm corresponding to the layer thickness. Such a unique microstructure was explained by local evaporation of alumina, but its effect on mechanical properties is not yet well understood. Liu et al. [68] used YSZ with a second laser for preheating (above 1500 °C) and observed that tetragonal phases are more common compared to the process in room temperature environment [69].

Gan et al. performed PBF-LB on a composite of alumina-spodumene powder. Spodumene formed the matrix around the alumina particles. EDS analysis before and after heat treatment at 900 °C showed that the matrix is changing from silicon rich to aluminum rich. In addition, alumina crystals are growing because of the heat treatment, which is explained by nucleation and crystal growth of spodumene around the alumina particles.

Wang et al. [94], Heinrich et al. [75], Mühler et al. [6] and Gahler et al. [7] found that both amorphous silica and mullite are produced when alumina and silica are laser processed. They mention that mullite needles could improve the fracture toughness of the parts. In [7], post heat treatment transformed the amorphous alumina in cristobalite and further enhanced the mullitization of silica in proximity of alumina. In addition, the same authors observed different microstructures within each layer, because of the different cooling rate at different depths.

Large columnar grains growing in the direction of building are commonly reported for the DED process by Balla et al. [17] and Niu et al. [14]. This has an important effect on the anisotropy of mechanical properties (see Section 4.3). The explanation for this phenomenon is that the main heat dissipation effect is through conduction to the substrate and the lower solidification rate compared to PBF-LB leads to larger grains. This microstructure facilitates the crack propagation, favoring vertical cracks. The primary spacing was about 60 μm and the length was in the order of hundreds of micrometers in Niu et al. [14] and

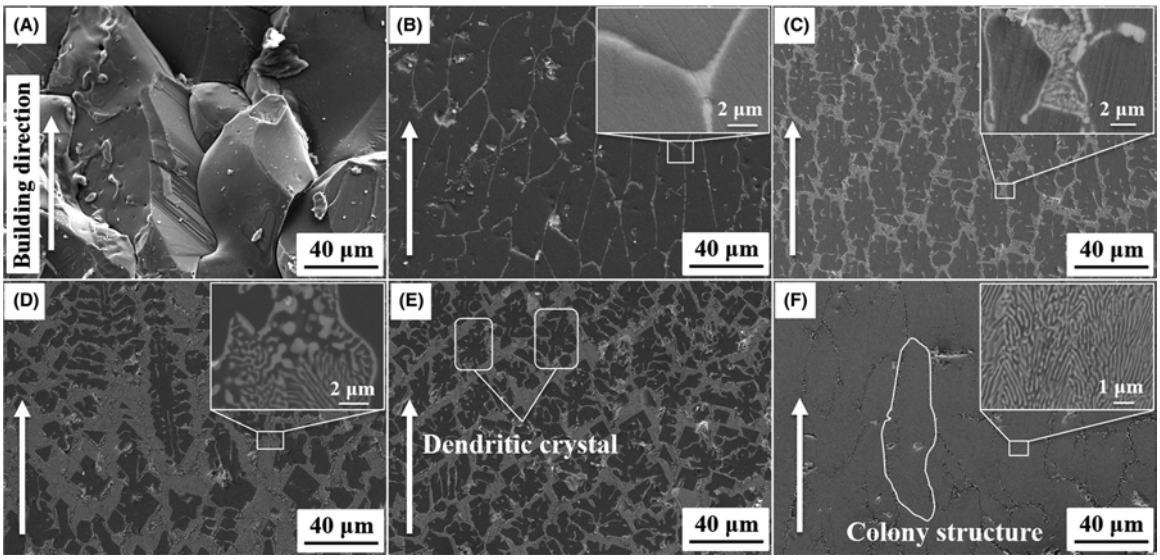

Fig. 15. Effect of zirconia doping on alumina microstructure. (A) pure alumina, (B) 6 wt% zirconia, (C) 12 wt% zirconia, (D) 23 wt% zirconia, (E) 34 wt% zirconia, (F) 42 wt% zirconia [133].

respectively 6.6 µm and tens of micrometers in Balla et al. [17]. The difference could be clearly explained by different laser parameters: Balla et al. used lower power and higher scan speed. These values are also significantly affected by heat treatment, which increased the grain size from 6.6 µm to huge grains of 207 µm in length [17].

Hu et al. showed that grain refinement could be achieved with ultrasonic vibration when 10 wt% YSZ doping was used (grain size reduced from 16 µm to 8 µm), which led to better mechanical properties (60 % higher compressive strength and 5% higher microhardness) [140, 144]. Eutectic alumina-zirconia phase was present at grain boundaries, but only zirconia was present at the boundaries when ultrasonic vibration was used.

YSZ doping (6 wt%) helped reducing the grain size to 15−18 µm, from around 50−100 µm in average for pure alumina [133]. Larger amount of YSZ led to finer alumina dendritic crystals surrounded by fine lamellar eutectic structures and finally only fine lamellar structures were obtained for the eutectic ratio. The effect of zirconia addition to alumina is clearly understood from Fig. 15 and it is comparable for all publications involving the same materials. A similar microstructure made of alumina grains surrounded by zirconia at the boundaries was obtained by Thakur and Pappas et al. [99,100] for YSZ-doping of alumina up to 10 wt%. Such structure is supposed to improve the crack resistance, because of crack bridging, deflecting and branching. However, other authors stated that a higher eutectic spacing could be also beneficial because of a more pronounced compressive stress toughening effect [145].

Yan et al. reported that the eutectic structure can be further refined and homogenized by ultrasonic vibration of the sample and substrate: the spacing could be reduced to 70 nm and the fracture toughness improved according to crack indentation measurements [137,138]. In addition, it was shown that both porosity and crack length could be minimized with appropriate choice of ultrasonic power [134]. Liu et al. studied the effect of scan speed on the microstructure and therefore a correlation between solidification rate and lamellar spacing was found [143].

Ma et al. showed that a banded structure is built in the building direction [145]. Bands with fine eutectic structure are interrupted by bands with large alumina grains, which forms because of the lower entropy of fusion of alumina. Yan et al. [146] analyzed the formation of banded structures and the influence of process parameters on them: they

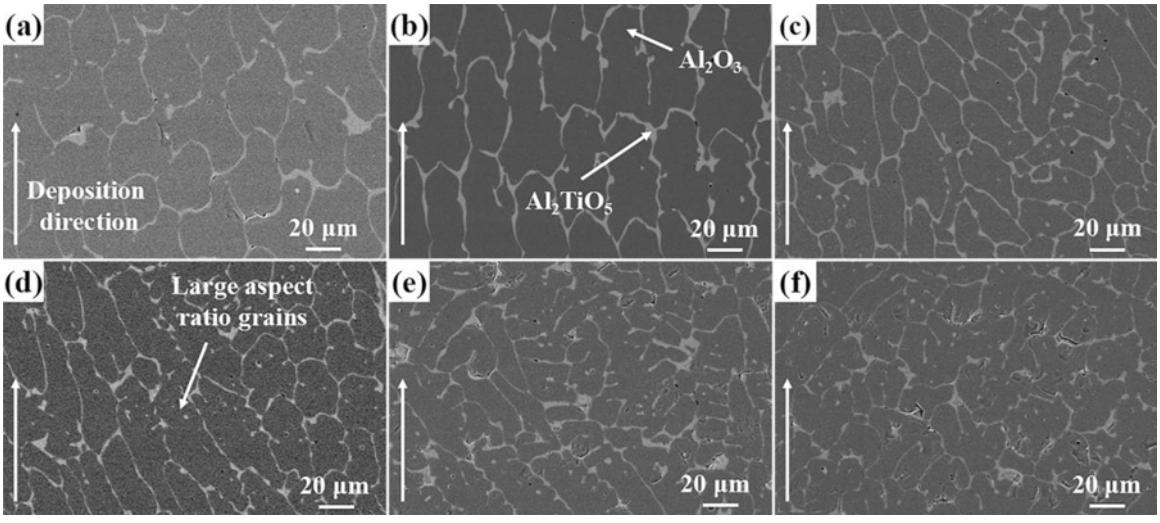

Fig. 16. Effect of scanning speed on microstructure of alumina-aluminum titanate composites: (a) 50 mm/min, (b) 100 mm/min, (c) 300 mm/min, (d) 500 mm/min, (e)700 mm/min, (f) 900 mm/min. [107].

could therefore minimize the banded structure to 10 μm and avoid independent nucleation. Furthermore, the use of ultrasonic power could achieve a thickness of only 2 μm for the banded zone by using ultrasonic vibrations [134]. Li et al. showed that a banded structure is formed along the building direction and the mean thickness of the bands is influenced by the energy input (power and speed) [156,157]. In addition, the microstructure also appeared different in the center and in the sides of the samples, because of the different cooling rates. At the center, the cooling rate is lower and this led to cellular structure compared to the columnar structure present at the borders.

Both spacing and fracture toughness were improved by addition of carbon fiber whiskers in [142]: spacing reached 50 nm and fracture toughness measured by crack indentation was 8.7 MPa $m^{1/2}$.

A stoichiometric mullite ratio of alumina and silica was tested in DED by Wu et al. [101]: mullite crystals of columnar shapes were created parallel to the building direction. The average spacing of 16.6 μm is reduced drastically near the edge, probably due to the different cooling rate. Silicon was predominantly detected at grain boundaries by EDS analysis, which may be a proof that a thin glass matrix was formed between the grains, explained by the fast cooling and the limited time for crystallization.

As explained in chapter 3, aluminum titanate can be generated in-situ during laser processing from a mixture of titanium dioxide and alumina. Al_2TiO_5 and also the peritectic phase $Al_6Ti_2O_{13}$ were mainly found as a matrix at α-alumina grain boundaries [14,148]. It was detected by a selected area electron diffraction analysis [107]. However, the difference in terms of crystal structure and physical properties of these phases is not relevant according to Niu et al. [14]. Grains showed a dendritic shape when the dopant amount exceeded 8 wt% and finally a fine lamellae structure of Al_2TiO_5 and $Al_6Ti_2O_{13}$ was formed for values near the eutectic. Alumina grain refinement was reported by Huang et al. [107] using higher scanning speed (Fig. 16).

Several attempts to produce parts with eutectic ratios with Al_2O_3 and Y_2O_3 powders showed the possibility of achieving fine eutectic microstructure, which prevents the formation of cracks [98,102]. Wu et al. [116] refined the eutectic microstructure in Al_2O_3-YAG with water cooling of the substrate, which generated dendritic structures with spacing down to 0.21 μm. Similar to Balla et al. [17], the dendritic growth direction occurred aligned to the build direction, since it followed the direction of the greatest thermal gradient (cooling through substrate). For the same material, Su et al. found that the scanning speed had a significant influence on the microstructure. Low speeds led to bigger eutectic spacing and a complex-irregular lamellar network, whereas higher speeds gave coarser zones with nanostructured intercellular zones due to constitutional supercooling and the high entropies of fusion of both phases [98].

Using the ternary eutectic made of alumina, YAG and zirconia, eutectic structures were dominant in the interior regions of the sample as well as on the bottom of each layer [16]. The appearance of colonies is attributed to a decreased thermal gradient to solidification rate ratio along the part building direction, which triggers cellular growth in colonies [161,162]. In contrary, in the outer regions of the sample, a regular and finer eutectic structure was present.

In Fan et al. [118] for the binary eutectic made of alumina and YAG, the microstructure changed from planar (big interphase spacing) to mainly cellular (small interphase spacing) with three interpenetrating phases along building direction. A transition from an irregular to a regular eutectic structure and a tilt of the cellular growth direction from parallel to a deviation up to 44° from build direction occurred at the boundary regions of the sample due to higher solidification rates.

Tables 3 and 4 summarize the observations that were done on the microstructure of LAM produced parts. It can be seen that a direct correlation with mechanical properties and density cannot be found, since other factors (such as presence of cracks) have an important impact. On the other side it can be noticed that the microstructure depends directly on material composition and process parameters, which define the cooling rate.

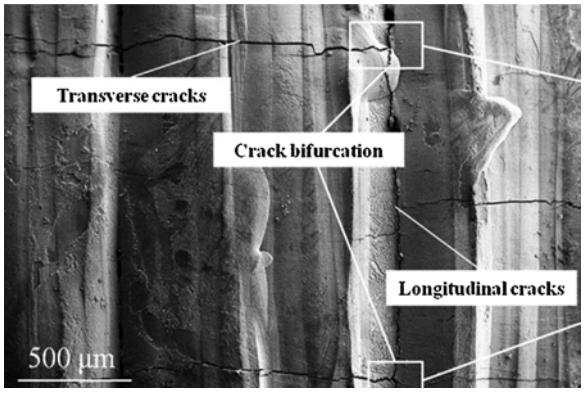

Fig. 17. Classification of cracks in PBF-LB: longitudinal cracks run along scan track boundaries, while transverse cracks run across scan tracks [15].

4.3. Mechanical properties

Common mechanical properties tests for LAM produced parts are:

- Bending strength with 3-point, 4-point, or ball-on-3-balls (B3B) bending test
- Compression strength
- Tensile strength
- Fracture toughness by indentation
- Hardness

Generally for ceramics, bending tests are the most appropriate, because tensile stresses are particularly critical for ceramics parts that therefore are usually designed with the criteria to avoid tensile stresses [61]. Indentation tests are proven to be a not reliable test for fracture toughness estimation since discrepancies were found with other standardized fracture toughness tests [163]. However, it may be used for comparison between different process parameters or materials as long as the microstructure is sufficiently homogeneous. Hardness by indentation is not a critical test for LAM-produced ceramics, because local hardness is high for large grains typically produced by these processes. This is especially the case for small indenters (nano- and micro-indenters) because they can involve small, local crack-free areas.

It is commonly agreed that cracks during LAM of ceramics are generated by the large thermal stresses that arise from rapid melting and re-solidification of the material. This limits considerably the mechanical strength of the produced parts and therefore also their applications in mechanically demanding applications.

Zhang et al. [76] and Zheng et al. [15] thoroughly analyzed cracks in PBF-LB of high performance ceramics and they both distinguished between transverse cracks, that are perpendicular to the scanning direction, and longitudinal cracks, that are parallel to the scanning direction as shown in Fig. 17. Zhang et al. noticed that transverse cracks were the most common within tracks and in the center of the specimen, while longitudinal cracks happened mainly between scan tracks [76]. Preliminary tests showed that the island scanning strategy could mitigate these problems. Zheng et al. noted that intergranular fractures along the columnar crystals are the most common, but transgranular cracks can also occur [15]. The predominant location of cracks in between granules was also reported by [26], while high resolution tomography performed by Pfeiffer et al. showed that cracks are mainly located along the vertical (build) direction [32]. The bi-axial flexural strength measured by the B3B test was only 25 MPa [22] (compression strength of 220 MPa), which are the highest values in the literature for PBF-LB-produced parts made of 99 % pure aluminum oxide.

Verga et al. showed that ATZ processing under atmosphere

(nitrogen) was beneficial for crack formation on the top surface of samples [29]. This was explained by the high-temperature reactions between oxygen in air and carbon, the dopant used to increase absorption. A 4-point bending strength was performed only for samples thermally post-treated at 1300 °C, because parts without heat treatment failed during preloading. The achieved bending strength was 31 MPa.

Juste et al. reported thermal treatments of the alumina PBF-LB-produced parts at 1550 °C were detrimental for mechanical properties: it generated additional cracks perpendicular to the building directions and did not reduce the porosity [25]. Possible reasons mentioned by the authors are related to residual stresses and gas evacuation resulting from reactions of the remaining graphite additive, used during the process for absorption enhancement. A beneficial effect was also not seen in [30] for alumina PBF-LB-produced parts heat treated at 1700 °C. This also proves that for alumina, differently than for ATZ, no shrinkage occurs because large cracks and pores cannot be removed with a post-treatment, since the distances are too big to be closed. The reason why ATZ may show a different behavior could be that phase transformation from tetragonal to monoclinic accompanied by volume expansion at crack tip occurs in zirconia.

The use of high temperature preheating by using a second laser and induction heating for alumina and zirconia ceramics in eutectic ratio is to date the only method that allowed to build parts of high mechanical strength [164] in PBF-LB. However, the required preheating temperature was above 1600 °C and the non-uniformity of temperature caused cracks due to different volume changes between top and bottom of the sample, especially in the case of bigger samples [165]. Mechanical strength was tested with B3B method for parts of only 0.6 mm in height and the achieved values were above 500 MPa with an average of 814 MPa. This value was close to the strength of traditional manufactured zirconia ceramics with a strength of 1000 MPa or higher [166].

Liu et al. proved that even with preheating up to 2500 °C cracks could not be avoided in YSZ using PBF-LB [68]. However, cracks were significantly reduced and became smaller and more disordered, especially above 2000 °C. The reason of these discrepancies may lie on the different material properties. Another reason can be the inhomogeneity of preheating, since large thermal gradients can be generated if the preheating is applied only on the top surface [68].

Another pre-heating option is offered by microwave. Buls et al. implemented a microwave-assisted PBF-LB process in a self-built machine made mainly in microwave-transparent quartz [18]. Crack-free parts were built but only for single tracks and single layers.

For PBF-LB with a CO_2 laser without pre-heating, the highest measured 4-point bending strength of components made from pure zirconia was only 9.8 MPa (5 samples) due to micro-cracks [84].

Exner et al. used a ceramic and glass composite to avoid crack formations in PBF-LB and reported a flexural strength of 100 MPa and compression strength of 800 MPa, which are similar to glass-related values [11,167]. The physical principle is that amorphous silica has a low thermal expansion coefficient: if partial melting of silica is achieved, then thermal stresses due to shrinkages during cooling are avoided [168]. By annealing of these parts [72], the bending strength was increased to 120 MPa (4-point bending method) and compression strength to 1150 MPa. The values are considerably lower than sintered high performance ceramic, but the ceramic and glass composite could still be an alternative to solid state sintering or melting of oxides for low demanding application. Bae et al. evaluated a hardness of 5.67 GPa for a composite made of 70:30 wt% glass based on SiO_2–B_2O_3–RO (R = Ba, Zn) to alumina [92]. The hardness is close to the values of glass [169] and much lower than that of alumina [170].

Using metal phases as starting material, which oxidizes in-situ during PBF-LB, is another alternative [96]. Mechanical properties were limited by delamination and four-point bending strength of the parts resulted in only 3.6 ± 0.7 MPa. This was most likely due to the low part density (45 %).

Regarding the hardness properties of high performance oxides, a value of 18.8 GPa was achieved on a YSZ single layer built with ultrashort pulsed laser in the femtosecond regime by Liu and Bai [13]. This value exceeded the hardness of an industrial made YSZ disk (13.7 GPa) and even of a YSZ single crystal (up to 16 GPa) [171].

Mapar claimed to have achieved crack free melting and resolidification by using a large spot of 760 μm, a high power of 900 W and speed of 400 mm/s, but the realized parts were extremely porous (about 30 % of porosity), showing that a larger spot and a combination of a relatively high power and low speed may lead to crack-free parts [66].

Indeed, Balla et al. [17] and Niu et al. [14] achieved crack-free alumina parts by DED, even though the built parts were only single walls and cylinders to contain thermal stresses. Grain growth was also reported leading to an increase in compressive strength and hardness after a post heat treatment at 1600 °C. The same authors also noticed that the strength in the direction normal to the build one is generally higher than in the build direction, because of the vertical grain orientation (Section 4.2). In [14], an average flexural strength of 210 MPa close to the values of conventionally manufactured high performance alumina [172] was measured, even though the variation of results was still relatively high (standard deviation of 91 MPa, however Weibull modulus was not given).

Regarding the processing parameters, Niu et al. showed that a scanning speed higher than 700 mm/min was beneficial for reducing the number of cracks in single-bead walls [110]. This was justified by the fact that time intervals between subsequent layers is smaller at high speed leading to smaller thermal gradients. In addition, high speed may have led to smaller grains, which lead to a microstructure more resistant to cracks. Such high speed may be however not suitable to avoid cracks in more complex and larger structures and lead to evident geometrical inaccuracies.

Titania mixed with alumina was also used to avoid cracks in more complex structures [14,107,148]. The working principle is that during the process aluminium titanate is formed, which is a material with low coefficient of thermal expansion and therefore suitable for withstanding thermal stresses. Cracks could be suppressed proportionally to the additive amount used up to 50 wt% [14]. However, due to the low mechanical strength of aluminum titanate, the best flexural strength was achieved for additive amounts below 10 wt% [148]. Higher amounts of aluminum titanate led to a strong decrease of flexural strength, hardness and fracture toughness accompanied by an increase of the porosity up to 5% [148]. A TiO_2 doping of 5 wt% [107] was proven to be the most suitable amount in terms of fracture toughness [148]. A trade-off between porosity at high scanning speed and cracks at low scanning speed was highlighted by [107] for cylinders of 5 mm in size: optimal properties were then established at medium scanning speed of 300 mm/min.

Wu et al. [101] reduced crack formation in alumina with the addition of SiO_2 in the mullite stoichiometric ratio. An in-situ formed mullite has a lower coefficient of thermal expansion. However, this was shown not to be sufficient to avoid cracks, which decreased drastically the mechanical properties (bending strength was limited to 62.8 MPa) [101]. This may be because mullite has lower mechanical strength than alumina [152].

The addition of YSZ to alumina helped reducing cracks [133]. It was shown that the optimal ratio for crack reduction is the eutectic composition (37 mol% of YSZ), similarly to what was already found for PBF-LB by Wilkes and Hagedorn [164,165]. Thakur et al. found an improvement in hardness with YSZ doping up to 10 wt% [99], while Hu et al. reported a maximum hardness for 20 wt% YSZ [144]. Wu et al. [135] analyzed even higher additive amounts. 20 mol% ZrO_2 showed similarly the highest hardness. However, eutectic ratio showed the highest flexural strength due to highest volume ratio of continuous eutectic structure matrix and materials with 60 mol% ZrO_2 had the highest fracture toughness due to phase transformation toughening effect. This increase in fracture toughness was confirmed by [157]. Pappas et al. measured the bending strength of 10 wt% YSZ-doped alumina in a 4-point bending test and the result was 208 MPa, while pure alumina

could achieve only 58 MPa [100].

Hu et al. achieved improved mechanical properties in an alumina-YSZ mixture (90 wt% alumina, 10 wt% YSZ) by the use of ultrasonic vibrations: the compressive strength increased from 280 MPa to 450 MPa [140]. This was achieved by the reduction of cracks and the refinement of grains. Li et al. found that a trade-off between fracture toughness and hardness exists. The maximum hardness was achieved for 15 wt% zirconia and lower heat input, while the maximum fracture toughness was achieved for 35 wt% zirconia and slightly higher heat input [157]. Hu et al. reported a reduction in cracks for DED produced parts when the laser power was increased from 325 W to 400 W [140]. According to Yan et al. laser power has the highest impact on part quality and the optimal parameters were found to be 420 W power, 400 mm/min scanning speed and 1.8 g/min feeding rate [139].

Fan et al. [118] built Al_2O_3–$Y_3Al_5O_{12}$–ZrO_2 ternary eutectics parts in DED without visible macro-cracks, but micro-cracks appeared at the bottom and top regions. Hardness of 18.9 GPa, fracture toughness of 3.8 MPa $m^{1/2}$ and elastic modulus of 367 GPa were very well comparable or even higher than properties of parts made with the same materials by the laser-heated floating-zone method [173].

4.4. Geometrical accuracy and surface quality

Achieving good accuracy and good surface quality is often problematic in LAM, due to the highly dynamic behavioursof the melting and solidification processes.

Liu et al. stated that an increase in energy density worsens the surface roughness and increased crack formation in PBF-LB [69]. These conditions are exacerbated in case of high temperature preheating. Wilkes et al. showed that melt often flowed out of intended contour during PBF-LB process at high temperatures, generating a very rough surface (roughness in the order of tens to few hundreds μm), which was considered not suitable for the intended dental application [20]. Similar problems were also found by [68] where a 2-laser preheating strategy was used and higher preheating temperature worsened the surface roughness.

Balling is also a typical problem in PBF-LB: it is caused by the relatively high surface tension of molten ceramics. Balling was avoided by [21,22] reducing the scanning speed, increasing the power and reducing the hatch space, which means increasing the energy density. Florio et al. also noticed that low repetition rate of 100 kHz would generate more balling than 300 kHz [22].

Juste et al. noticed that PBF-LB processed parts with regular shapes had low density, while parts with higher density exhibited a concave upper surface [25]: the authors explained this with the high recoil pressure generated during the process.

Gan et al. experienced cracks and delaminations at the part-substrate interface, due to high thermal gradients [70]. This phenomenon was most evident for a layer thickness of 50 μm, which is also the parameter value that delivered the highest density. Delaminations were avoided by Verga et al. coating a thin layer of soldering alloy Sn60Pb40 on a steel plate [29]. This may be the result of better heat conduction of the substrate and improved interface strength between built part and substrate. In addition, removal of parts from the substrates was relatively easier, since it is then possible to heat the soldering alloy up to its melting temperature in order to remove the produced parts. Caprio et al. [174] also pointed at the importance of the substrate for processing of regolith by PBF-LB. In this case, refactory clay performed better than carbon steel, since it chemically similar. In the case of carbon steel, powder and baseplate were chemical incompatible and thus the laser interacted directly with the substrate and caused powder spreading and denudation.

Roughness below Ra 5 μm were reported by Exner et al. [72] using a green pulsed laser and an experimental setup in which fine powder was compressed before the PBF-LB process. Wilkes and Wissenbach achieved Ra 12 μm with a standard CO_2 laser in the surfaces parallel to the building direction and 2 μm in the perpendicular one [83].

The geometrical accuracy and surface properties are generally worse in DED, because the laser beam spot size is about 1 order of magnitude larger compared to PBF-LB, as shown in the Tables 1 and 2. In particular, the beam spot size clearly reduce the geometrical freedom, since features smaller than the beam spot size cannot be realized.

Li et al. analyzed the effect of different process parameters on geometrical accuracy and surface roughness of samples produced in DED [112]. They noticed a positive effect on surface roughness and flatness when the power was higher because of the reduction of unmolten particles and of the decrease in viscosity of the melt pool. Larger scanning speed resulted in an increase in the surface roughness, while the flatness of the whole layer improved.

Crack-free structures of eutectic alumina-zirconia up to 230 mm in length and rather complex 3D-structures were built by [133] in DED. However, surface roughness and geometrical accuracies were not assessed.

5. LAM process monitoring and material characterization - in-situ sensing and metrology

The layer-wise production paradigm of LAM processes potentially makes a large amount of data available during the process by using in-situ installed sensors like powder bed camera, co-axial pyrometers, high-speed cameras and thermal cameras. The values that can be measured are called “process signatures” [175] and can be used as proxies of both the process stability over time and the onset of defects and anomalies in the part. In this field, a distinction can be made between “in-situ sensing”, “in-situ metrology” and “in-situ monitoring” methods. The term “in-situ sensing” refers to the acquisition of signals by using in-situ installed sensors. The term “in-situ metrology” refers to the ability of measuring one or more quantities of interest based on in-situ gathered signals. The term “in-situ monitoring” refers to the ability of detecting errors, defects and anomalous process states through machine learning and/or automated alarm rules while the part is being built.

So far, the highest maturity of in-situ metrology solutions has been achieved in metal PBF processes, where hundreds of studies have been published and commercial toolkits are available from industrial system

Table 5
Measured process signatures and in-situ sensing methods.

Measured signature		Reference	Material	Sensor	Temporal resolution
Level 1	Denudation zone	Puccio et al. [182]	Al_2O_3 doped with Fe_2O_3 and MnO_2	High-speed camera	
Level 2	Heating and cooling profiles	Liu et al. [68]	Y_2O_3 stabilized ZrO_2	Thermal camera	–
	Process by-products	Lacertosa et al. [183]	Al_2O_3 doped with Fe_2O_3	High-speed camera	1000−15000 fps
Level 3	Melt pool radiation spectrum	Qian et al. [184]	Al_2O_3	Spectrometer	–
	Melt pool intensity	Qian et al. [184]	Al_2O_3	Pyrometer	–
		Zhang et al. [185]		Photodiode	–
		Puccio et al. [182]	Al_2O_3 doped with Fe_2O_3 and MnO_2	Photodiode	–
	Melt pool morphology	Qian et al. [184]	Al_2O_3	High-speed camera	30 fps
	Melt pool size	Puccio et al. [182]	Al_2O_3 doped with Fe_2O_3 and MnO_2	High-speed camera	5000 fps

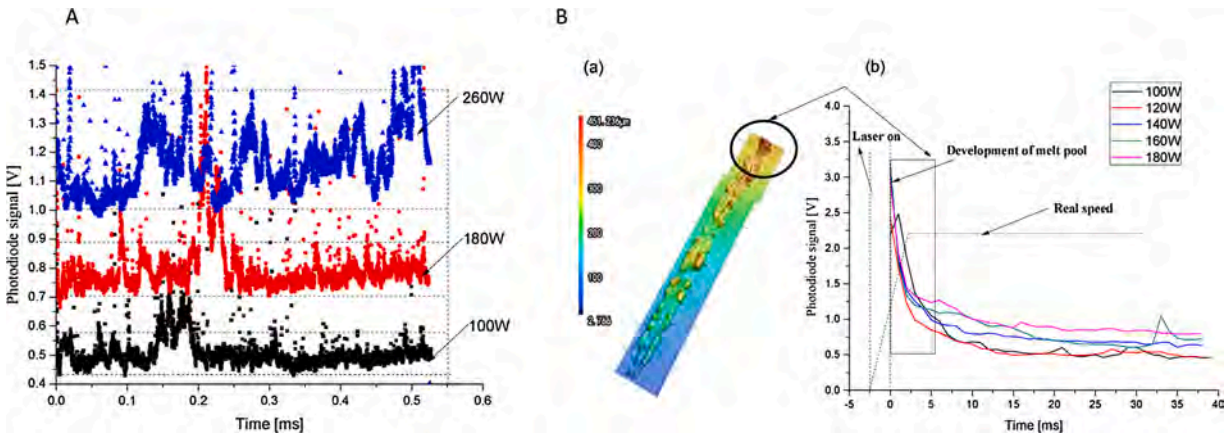

Fig. 18. Examples of photodiode signals for different laser power levels (A) and at the beginning of single track scanning (B) from Zhang et al. [185].

developers [176–178]. Several in-situ sensing and metrology techniques have been proposed and validated in laser and electron beam metal PBF processes. Major research efforts are currently devoted to the development of in-situ monitoring tools suitable to make sense of big data streams to detect defects and anomalies and, when possible, activate closed-loop control or in-situ defect correction strategies for defect avoidance or removal [179–181].

In the framework of LAM processes for ceramic materials, only few authors investigated the potentials of in-situ sensing and metrology to characterize the laser-material interaction and as support tools to accelerate material development, process tuning and optimization.

Similarly to classifications proposed in the mainstream literature devoted to metal AM [176–178], it is possible to group in-situ sensing and metrology methods into three main levels depending on the measured quantity. Level 1 includes quantities that can be measured by looking at the entire powder bed before and/or after the melting phase. This approach is applicable only in PBF processes, where high spatial resolution images of the powder bed can be acquired in each layer. Level 2 involves the measurement of quantities related to beam-material interactions during the scan of each track. Information about heating and cooling profiles can be gathered through high-speed measurements focused on the melting phase, as well as local heat accumulations and process by-products like spatters and plume emissions. Level 3 involves high-speed measurements of salient melt pool properties like radiation intensity, size, shape and temperature profiles.

Table 5 summarizes and classifies the literature on in-situ sensing and metrology of LAM processes for high performance oxide ceramics. All studies were carried out in PBF-LB and in all of them alumina powder was used with the only exception of Liu et al. [68]. In terms of sensing equipment and configuration, all reviewed studies adopted off-axis mounted sensors, including high-speed cameras, thermal cameras and spatially integrated pyrometers.

In-situ data acquisition during the PBF-LB of oxide ceramics was first adopted and investigated in a few seminal studies [19]. Hagedorn et al. also demonstrated the production of dense specimens from the eutectic mixing ratio of 58.5 wt% of Al_2O_3 and 41.5 wt% ZrO_2, where crack formation was avoided by high-temperature preheating [19]. An off-axis mounted thermal camera was used to observe the heat map evolution during pre-heating and melting phases. In-situ metrology was only used to support the experimental definition of preheating temperatures. Hagedorn et al. [19] showed a poor surface quality of produced parts, which was studied in more depth in Hagedorn et al. [165], where an off-axis high-speed video imaging was used. In-situ high speed videos showed the ceramic melt flowing out across the boundaries of the slice leading to the rough surface pattern observed on produced specimens. Hagedorn et al. pointed out that a too large melt pool volume could be the root cause of this observed phenomenon [165].

A similar in-situ sensing setup was used by Liu et al. [68] in PBF-LB of yttria stabilized zirconia ceramic. An off-axis thermal camera was used to measure the average temperature in the layer and the average temperature profile along time for different pre-heating temperatures in the range 1500 °C–2500 °C. Liu et al. [68] discussed the link between the temperature history and the formation of irregular pores and cracks. They linked i) the presence of smaller pores in the centre of the specimens to the extremely short cooling time that prevents air in the interstices of the powder to leave the material, and ii) the presence of horizontal cracks to the difference of temperature and cooling speed between the inner region of the specimens and the contours.

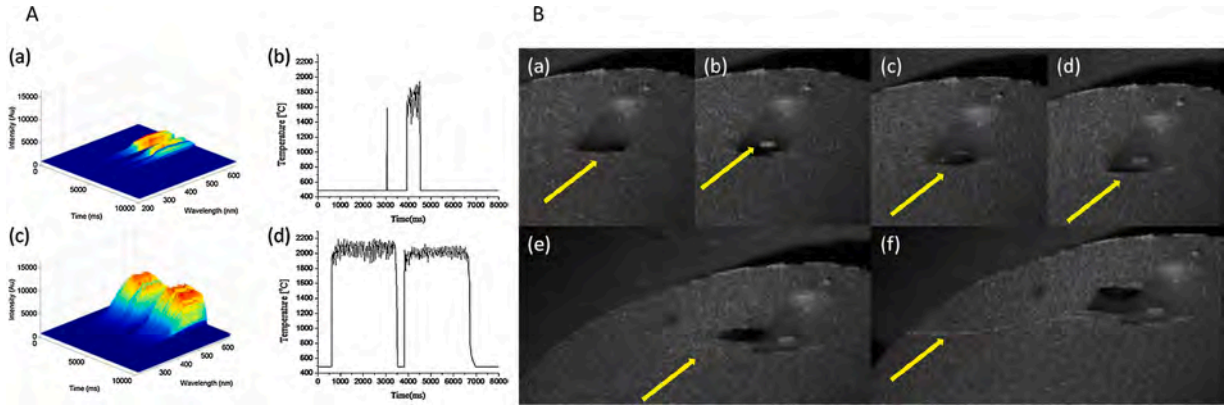

Fig. 19. Examples from Qian et al. [184]. A: examples of spectrometer (a, c) and pyrometer (b, d) signals for two different energy inputs; B: in-situ measured time evolution of two defects (poorly consolidated powder (a- d) and crack formation (e, f)).

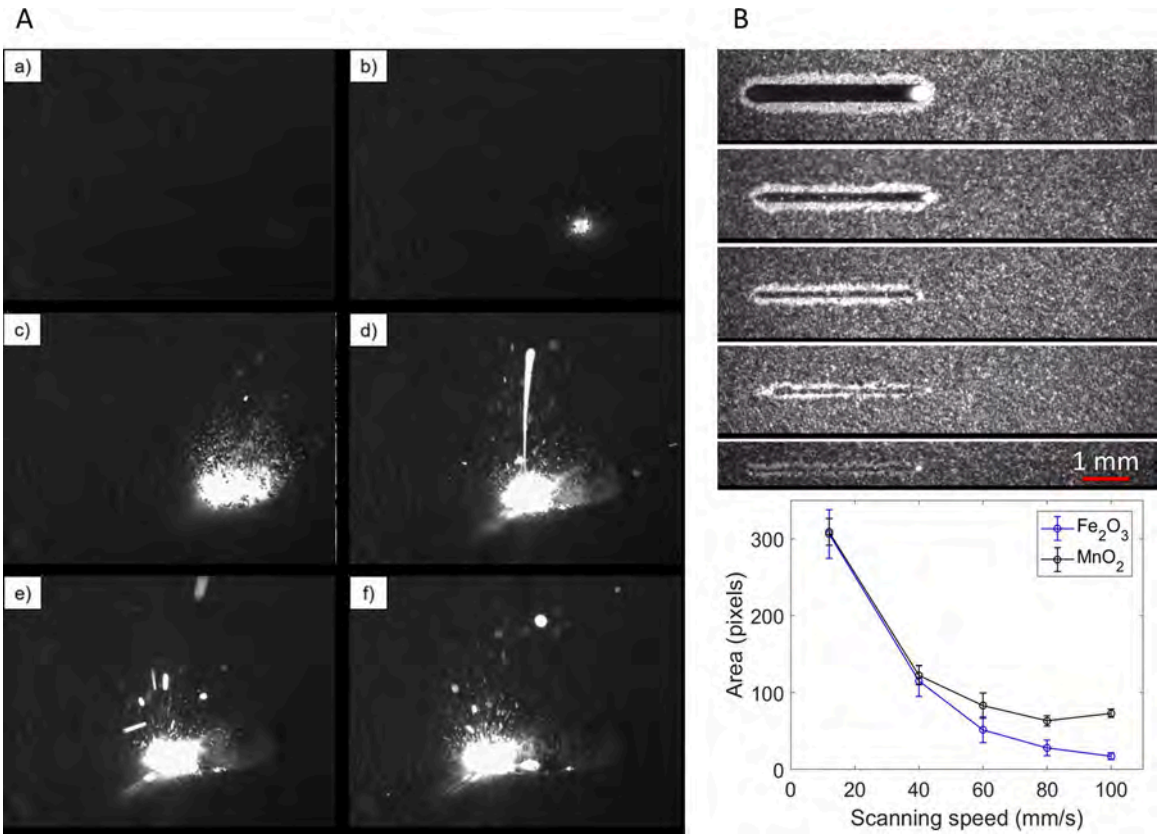

Fig. 20. Examples of spatter ejections from Lacertosa et al. [183] (A) and correlation between in-situ measured melt pool area and scan speed in Puccio et al. [182] (B).

More recent studies made a more quantitative use of in-situ gathered data to characterize observed phenomena and to tune the process. Zhang et al. [185] developed an in-situ monitoring equipment for the PBF-LB of Al_2O_3 consisting of multiple off-axis mounted photodiodes. The build area was divided into several square regions with equal area and one photodiode was allocated to each of them. Photodiodes were aligned in order to ensure equal distances from the target sub-region and equal angles above the build area for all the sensors. All photodiodes had a measurement bandwidth of 850–960 nm. The rationale behind this in-situ sensing configuration is that using one single off-axis photodiode would lead to measurement biases depending on the melt pool location within the build area, as a consequence of different distances and angles from the photodiode. This problem was overcome thanks to the proposed multi-detection apparatus. Zhang et al. [185] showed that increasing the laser power caused not only an increase of the radiation intensity measured by the photodiodes, but also bigger signal fluctuations (Fig. 18). Melt pool intensity variations were correlated to the quality of the track. Photodiode signals also revealed differences between internal hatches and contours as well as melt pool behavior at the beginning of each track linked to the time needed by the galvanometric scanner to reach the set point of scan speed. Zhang et al. [185] pointed out that the presented results could drive the selection of optimal process parameters and that local anomalies (i.e., at the beginning of each track and in the interface between internal hatches and contour tracks) could be mitigated by means of closed-loop control strategies.

Qian et al. [184] presented an in-situ metrology approach in PBF-LB of alumina consisting of two different off-axis mounted sensors, i.e., an high-speed camera in the visible range and a pyrometer. The pyrometer was used to measure both the integrated emitted radiation intensity and its spectral properties in the wavelength interval from 200 nm to 600 nm. The spectrometer was used to identify a heat input interval with narrow signal fluctuations, which reflected into a more stable sintering process (Fig. 19**A**). The pyrometer signals were used to characterize local heating patterns for different energy inputs. The high-speed camera was used to illustrate the quality of consolidated layers and to investigate the onset of defects and their origination mechanisms (Fig. 19**B**).

Two recent studies further investigated the use of high-speed video imaging for the analysis of melt pool size and process by-products in PBF-LB. Preliminary results showed in the master thesis of Lacertosa et al. [183] suggest that spatters, produced by emissions of liquid material from the melt pool, can be possibly used as proxies of the process stability also in PBF-LB of ceramics (Fig. 20**A**). Spatters were shown to be drivers of process instability in metal PBF-LB (Repossini et al. [186]), as their behaviour is affected by process parameters and ambient conditions. Puccio et al. [182] studied in-situ measurements in PBF-LB of Al_2O_3 doped with Fe_2O_3 and MnO_2 by using two sensing method to characterize the major differences between the two materials. A high-speed video imaging was used to estimate the size of the denudation zone and the melt pool and how they are affected by different scan speeds (Fig. 20**B**). An integrating sphere equipped with a photodiode to measure the absorptivity along single track scans.

This section highlights that various kinds of in-situ gathered data may enclose relevant information about the laser-material interaction and the onset of defects. They can be used to support the development of LAM processes optimized for high performance and fully dense oxide ceramic parts, providing insights about defect origination mechanisms and process stability variations caused by different energy density levels. In this framework, some challenges to be tackled are specific to ceramics, like the low absorptivity of the material. However, fundamental papers and more recent studies demonstrated that by using ad-hoc illumination settings and appropriate optical equipment, in-situ sensing and metrology methods that are quite mature in metal AM can be effectively used in LAM of ceramics as well.

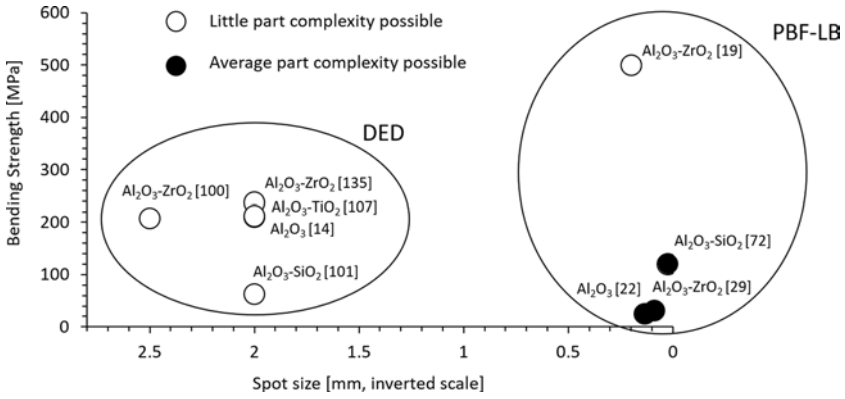

Fig. 21. Trade-offs between mechanical strength, accuracy (beam size) and complexity of parts.

6. Potential developments, applications and conclusions

Various future developments are needed to enhance LAM process capabilities and to tackle all the challenges discussed in previous chapters. Several works have been already focused on process parameter optimization and quality improvement as seen in the previous chapters. However, new approaches are necessary to expand the possibilities of LAM of high performance oxide ceramics to combine high mechanical properties with good part accuracy in complex parts. Fig. 21 shows how DED and PBF-LB are complementary in this regard. PBF-LB allows to build more complex parts with higher accuracy using a smaller spot size, such as those shown in Fig. 5. On the other side, the large beam of DED is useful to avoid crack formation and to achieve higher mechanical strength. The results from Hagedorn [165] are an outlier. Parts with high strength could be built in PBF-LB because of the extreme high temperature pre-heating, but they were limited in the vertical dimension to less than 2 mm.

Currently, the only approach to have dense and crack-free parts with high mechanical strength are the combination of PBF-LB with high temperature pre-heating (above 1600 °C) or the DED process. However, in both cases the feasible geometries are limited. In the case of PBF-LB, the uniformity of the extreme high temperature preheating is the main challenge, which must be improved to allow the build of larger and more complex structures. EBM could also offer a possibility to generate a high temperature preheating, but the electrical charging of powder should be taken into account, in case non-electrically conductive materials are used. Furthermore, minimum beam diameter is slightly bigger (250 μm) than in PBF-LB [187,188]. Implementation of dopants as shown in [25,30,32] could be a solution to improve the electrical conductivity and thus finally the part properties.

DED of ceramics could already be an option today to build thin-walled structures or cylinders for materials that need to be solidified from the molten state. More complex structures would cause large thermal gradients within the parts even when a large laser spot size is used. Also in the case of DED, an improvement of preheating strategies could be useful to avoid cracks in larger parts.

However, dimension control is an open challenge in DED. The large spot size and the uncontrolled layer thickness are typical challenges of DED. Bending strength was measured only for parts built with a spot size larger than 2 mm (Tables 2 and 4), which limits the accuracy and surface roughness. Power prediction models such as the one in Niu et al. [111], closed-loop controls and a combination of the two approaches can help improving the uniformity of layer thickness and increase accuracy, similar to what was already proven for metal DED [189].

An application of complex high performance oxidic parts produced via LAM could be found in advanced casting of ceramic molds for casting of metals. The advantages would be a controllable porosity, a high freedom of design and to avoid a time-intensive temperature profile.

LAM offers the chance to produce graded oxidic structures with a hard and dense core surrounded by layers of gradually lower hardness and density. This requires the variation of densities between consecutive layers as well as in-plane variations within several layers. The opportunity exists to combine this with a corner or concave radius. When pieced together, more more complex geometric shapes are formed. This three-dimensional structure with a dense bulk ceramic structure and a surface porosity are typically applied in dental ceramic implants.

The need to avoid cracks reducing thermal stresses is often in contrast with the need for a fine microstructure. As seen in the authors previous work and by other authors, melting processes in LAM lead to the crystal growth for pure alumina because the cooling rate is relatively low [26]. This phenomenon will in consequence weaken the mechanical properties of the laser-processed parts leading to decreased fracture toughness.A solution for the problem could be the addition of different oxide dopants, which are known to decrease the grain growth for certain materials (e.g. cobalt oxide, nickel oxide, magnesium oxide, barium oxide, sodium oxide etc. for aluminum oxide [190]) or to adjust the laser parameter to achieve a high cooling rate. On the other hand, large grains are beneficial for high temperature applications due to reduced creep rate, which could be a chance for LAM to find a future application field in this sector. Furthermore, dopants could be used to generate nucleation from the melt during solidification. However, the use of dopants also changes the physics of the process completely and lead thus to difficult process adjustments.

Post processing of the parts could be another possibility. Wilkes and Wissenbach suggested an infiltration of the cracks by molten glass and the use of hot isostatic pressing for crack healing of selective laser melted samples [83]. However, to infiltrate cracks by glass the glass melt needs to have a low viscosity (adjustable by temperature or additives) and the part needs to have a reasonable amount of open porosity for full infiltration. Lee et al. [90] infiltrated laser manufactured alumina-glass composites with colloidal silica and thermally annealed the parts. The strength increase was 3–5 MPa due to porosity reduction. Hot isostatic pressing is promising, but its efficacy in closing relatively large cracks needs to be proven. Furthermore, it is a time-intensive and expensive option. Similar to this method, Ceracon forging was applied to further densify laser processed parts [89]. Instead of the gaseous medium in hot isostatic pressing, a particulate material is used to transmit pressures up to 1400 MPa [191]. The 4-point strength of the alumina glass composites reached values up to 110 MPa after full densification. However, the shrinkage due to strong densification in this process was up to 59 % [89], which is counter-productive for a near-net-shape fabrication aimed in LAM.

Finally, another option for improving the current processes is to develop materials that are better suitable for LAM processes. Materials with low or negative thermal expansion coefficient, high tensile strength and high fracture toughness are desirable for withstanding thermal stresses. These properties could be achieved also through the realization of composites, as for instance was done by Wu et al. adding SiC particles

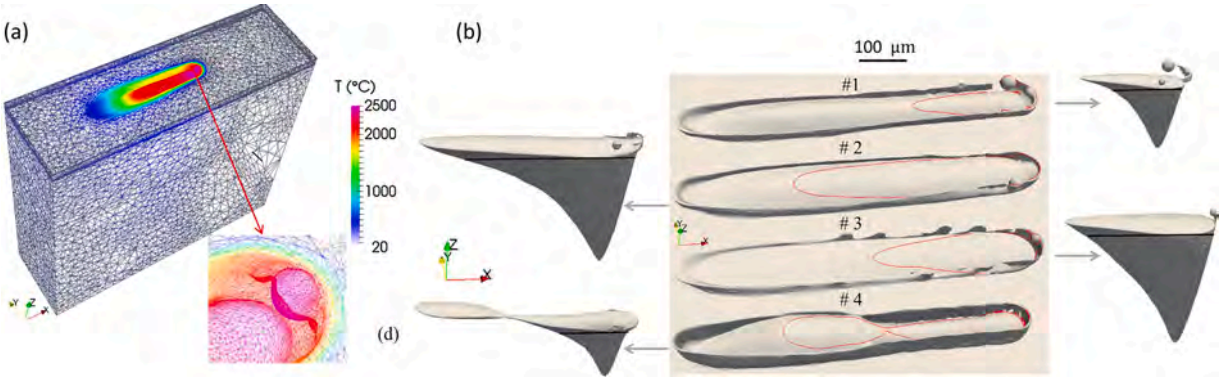

Fig. 22. Examples from Chen et al. [196]. (a) FE mesh adaptation at the vicinity of the melt pool surface and temperature field; (b) simulated bead shape (center) and melt pool shape (two sides) for 4 different cases. The black line drawn on the melt pools is the powder/substrate boundary.

[141]. Inclusion of nanofibers or whiskers could be another solution to improve this properties, as already shown for oxide matrices with addition of oxide fibers [192,193]. Furthermore, carbide or nitride fibers could be interesting in the case of LAM. However, issues with powder handling have to be expected.

One future research direction of potential interest for the development and tuning of LAM of high-performance oxide ceramics involves the use of process modelling and simulation tools. So far, only few authors investigated the benefits of finite element modelling (FEM) in this framework. The seminal study of Li et al. [194] developed a 3D-FEM approach in PBF-LB of alumina-based refractory ceramics to investigate the temperature distribution of the melt pool and its surrounding area and the related thermal stress field. The authors showed that process simulation could provide insights about crack density and location within the part. More recent studies were conducted by Chen et al. [195, 196], who simulated the PBF-LB process of alumina at track scale, studying the influence of process parameters and material properties (Fig. 22B). Chen et al. [196] used a dynamic mesh adaptation to capture the material/gas interface evolution and simulated the melt pool shape for different process parameters (Fig. 22A). One of the main limitations of these studies is the lack of a deep understanding of optical properties, especially regarding doped powder and powder composed of different phases, which limits the accuracy in the definition of the input power.

A more recent study from the same authors [195] introduced the Marangoni force at the gas/liquid and powder/liquid interfaces into the model. The Marangoni effect on the temperature distribution of the melt pool was investigated and related to the height of the solidified track, track fragmentation and associated balling effect.

3D-FEM and other more advanced simulative tools, such as meshless methods, are a potential tool to understand the process dynamics, enabling the possibility of accelerating the development of LAM processes for dense and high performance ceramics, similar to what happened for metals [197–199]. However, there is limited literature in this field and a lack of consolidated methods. Model validation is an open issue too, like for AM of other materials. Coupling simulation results with in-situ gathered observations may represent a research field where new developments may be of great interest.

It is finally clear that a co-development of materials and processes is needed to reduce thermal stresses and thus the cracking issue, similarly to what happened in other fields of manufacturing. Modelling and experimental works should support each other and thus limitations of both approaches should be overcome, in order to find suitable combinations of materials and processes.

Declaration of Competing Interest

The authors declare that they have no known competing financial interests or personal relationships that could have appeared to influence the work reported in this paper.

Acknowledgements

An exceptional thank goes to the ETH Board for funding the “FUORCLAM” project within the frame of the SFA (Strategic Focus Area) Advanced Manufacturing. The authors thank Dr. Jon Bell and Dr. Sathya Narayanasamy for proofreading the text.

References

[1] A.J. Pinkerton, Lasers in additive manufacturing, Opt. Laser Technol. 78 (2016) 25–32.
[2] T. Wohlers, R.I. Campbell, O. Diegel, R. Huff, J. Kowen, Wohlers Report 2020: 3D Printing and Additive Manufacturing State of the Industry Wohlers Associates Fort Collins, CO2020.
[3] T. Moritz, S. Maleksaeedi, Additive manufacturing of ceramic components, in: J. Zhang, Y.-G. Jung (Eds.), Addit. Manuf., Butterworth-Heinemann, 2018, pp. 105–161.
[4] Z. Zhang, M.F. Modest, Temperature-dependent absorptances of ceramics for Nd: YAG and CO2 laser processing applications, J. Heat Transfer 120 (2) (1998) 322–327.
[5] V.A. Petrov, Abrupt increase of the absorption coefficient of alumina at melting by laser radiation and its decrease at solidification, Int. J. Thermophys. 30 (6) (2009) 1938–1959.
[6] T. Mühler, C.M. Gomes, J. Heinrich, J. Günster, Slurry-based additive manufacturing of ceramics, Int. J. Appl. Ceram. Technol. 12 (1) (2015) 18–25.
[7] A. Gahler, J.G. Heinrich, J. Günster, Direct laser sintering of Al2O3-SiO2 dental ceramic components by layer-wise slurry deposition, J. Am. Ceram. Soc. 89 (10) (2006) 3076–3080.
[8] Y. Wu, J. Du, K.-L. Choy, L.L. Hench, Laser densification of alumina powder beds generated using aerosol assisted spray deposition, J. Eur. Ceram. Soc. 27 (16) (2007) 4727–4735.
[9] J. Deckers, S. Meyers, J.P. Kruth, J. Vleugels, Direct selective laser sintering/melting of high density alumina powder layers at elevated temperatures, Phys. Procedia 56 (2014) 117–124.
[10] H. Exner, P. Regenfuß, R. Ebert, L. Hartwig, A. Streek, S. Klötzer, M. Horn, Lasermikrosintern von keramischen Materialien, RTeJournal 3 (3) (2006).
[11] P. Regenfuss, A. Streek, L. Hartwig, S. Klötzer, T. Brabant, M. Horn, R. Ebert, H. Exner, Principles of laser micro sintering, Rapid Prototyping J. 13 (4) (2007) 204–212.
[12] Z. Fan, M. Lu, H. Huang, Selective laser melting of alumina: a single track study, Ceram. Int. 44 (8) (2018) 9484–9493.
[13] J. Liu, S. Bai, Femtosecond laser additive manufacturing of YSZ, Appl. Phys. A 123 (4) (2017).
[14] F. Niu, D. Wu, F. Lu, G. Liu, G. Ma, Z. Jia, Microstructure and macro properties of Al2O3 ceramics prepared by laser engineered net shaping, Ceram. Int. 44 (12) (2018) 14303–14310.
[15] Y. Zheng, K. Zhang, T.T. Liu, W.H. Liao, C.D. Zhang, H. Shao, Cracks of alumina ceramics by selective laser melting, Ceram. Int. 45 (1) (2019) 175–184.
[16] Z. Fan, Y. Zhao, Q. Tan, N. Mo, M.-X. Zhang, M. Lu, H. Huang, Nanostructured Al2O3-YAG-ZrO2 ternary eutectic components prepared by laser engineered net shaping, Acta Mater. 170 (2019) 24–37.
[17] V.K. Balla, S. Bose, A. Bandyopadhyay, Processing of bulk alumina ceramics using laser engineered net shaping, Int. J. Appl. Ceram. Technol. 5 (3) (2008) 234–242.
[18] S. Buls, J. Vleugels, B. Van Hooreweder, Microwave assisted selective laser melting of technical ceramics, in: Annual International Solid Freeform Fabrication Symposium - an Additive Manufacturing Conference, 29, 2018, pp. 2349–2357.

[19] Y.-C. Hagedorn, J. Wilkes, W. Meiners, K. Wissenbach, R. Poprawe, Net shaped high performance oxide ceramic parts by selective laser melting, Phys. Procedia 5 (2010) 587–594.
[20] J. Wilkes, Y.C. Hagedorn, W. Meiners, K. Wissenbach, Additive manufacturing of ZrO2-Al2O3 ceramic components by selective laser melting, Rapid Prototyping J. 19 (1) (2013) 51–57.
[21] Y.-D. Qiu, J.-M. Wu, A.-N. Chen, P. Chen, Y. Yang, R.-Z. Liu, G. Chen, S. Chen, Y.-S. Shi, C.-H. Li, Balling phenomenon and cracks in alumina ceramics prepared by direct selective laser melting assisted with pressure treatment, Ceram. Int. 46 (9) (2020) 13854–13861.
[22] K. Florio, S. Pfeiffer, M. Makowska, N. Casati, F. Verga, T. Graule, H. Van Swygenhoven, K. Wegener, An innovative selective laser melting process for hematite-doped aluminum oxide, Adv. Eng. Mater. 21 (6) (2019).
[23] P. Bertrand, F. Bayle, C. Combe, P. Goeuriot, I. Smurov, Ceramic components manufacturing by selective laser sintering, Appl. Surf. Sci. 254 (4) (2007) 989–992.
[24] B. Qian, Z. Shen, Laser sintering of ceramics, J. Asian Ceram. Soc. 1 (4) (2013) 315–321.
[25] E. Juste, F. Petit, V. Lardot, F. Cambier, Shaping of ceramic parts by selective laser melting of powder bed, J. Mater. Res. 29 (17) (2014) 2086–2094.
[26] L. Ferrage, G. Bertrand, P. Lenormand, Dense yttria-stabilized zirconia obtained by direct selective laser sintering, Addit. Manuf. 21 (2018) 472–478.
[27] S. Chang, L. Li, L. Lu, J.Y.H. Fuh, Selective laser sintering of porous silica enabled by carbon additive, Materials 10 (11) (2017).
[28] L. Moniz, C. Colin, J.-D. Bartout, K. Terki, M.-H. Berger, Laser beam melting of alumina: effect of absorber additions, JOM 70 (3) (2018) 328–335.
[29] F. Verga, M. Borlaf, L. Conti, K. Florio, M. Vetterli, T. Graule, M. Schmid, K. Wegener, Laser-based powder bed fusion of alumina toughened zirconia, Addit. Manuf. 31 (2020).
[30] S. Pfeiffer, K. Florio, M. Makowska, D. Ferreira Sanchez, H. Van Swygenhoven, C. G. Aneziris, K. Wegener, T. Graule, Iron oxide doped spray dried aluminum oxide granules for selective laser sintering and melting of ceramic parts, Adv. Eng. Mater. 21 (6) (2019).
[31] X. Zhang, S. Pfeiffer, P. Rutkowski, M. Makowska, D. Kata, J. Yang, T. Graule, Laser cladding of manganese oxide doped aluminum oxide granules on titanium alloy for biomedical applications, Appl. Surf. Sci. 520 (2020), 146304.
[32] S. Pfeiffer, M. Makowska, F. Kevin, D.F. Sanchez, F. Marone, X. Zhang, C. G. Aneziris, H. Van Swygenhoven, K. Wegener, T. Graule, Selective laser melting of thermal pre-treated metal oxide doped aluminum oxide granules, Open Ceram. (2020), 100007.
[33] N. Travitzky, A. Bonet, B. Dermeik, T. Fey, I. Filbert-Demut, L. Schlier, T. Schlordt, P. Greil, Additive manufacturing of ceramic-based materials, Adv. Eng. Mater. 16 (6) (2014) 729–754.
[34] J.-C. Wang, H. Dommati, S.-J. Hsieh, Review of additive manufacturing methods for high-performance ceramic materials, Int. J. Adv. Manuf. Technol. 103 (5-8) (2019) 2627–2647.
[35] J. Deckers, J. Vleugels, J.-P. Kruth, Additive manufacturing of ceramics: a review, J. Ceram. Sci. Technol. 5 (4) (2014) 245–260.
[36] S.L. Sing, W.Y. Yeong, F.E. Wiria, B.Y. Tay, Z. Zhao, L. Zhao, Z. Tian, S. Yang, Direct selective laser sintering and melting of ceramics: a review, Rapid Prototyp. J. 23 (3) (2017) 611–623.
[37] A.-N. Chen, J.-M. Wu, K. Liu, J.-Y. Chen, H. Xiao, P. Chen, C.-H. Li, Y.-S. Shi, High-performance ceramic parts with complex shape prepared by selective laser sintering: a review, Adv. Appl. Ceram. 117 (2) (2018) 100–117.
[38] D. Grossin, A. Montón, P. Navarrete-Segado, E. Özmen, G. Urruth, F. Maury, D. Maury, C. Frances, M. Tourbin, P. Lenormand, G. Bertrand, A review of additive manufacturing of ceramics by powder bed selective laser processing (sintering / melting): calcium phosphate, silicon carbide, zirconia, alumina, and their composites, Open Ceram. 5 (2021), 100073.
[39] Y. Hagedorn, 6 - laser additive manufacturing of ceramic components: materials, processes, and mechanisms, in: M. Brandt (Ed.), Laser Additive Manufacturing, Woodhead Publishing, 2017, pp. 163–180.
[40] I. Astm, ASTM52900-15 Standard Terminology for Additive Manufacturing—General Principles—Terminology, ASTM International, West Conshohocken, PA, 2015.
[41] J.J. Beaman, C.R. Deckard, United States Patent 4938816, United States Patent 4938816 (1990).
[42] A. Zocca, P. Colombo, C.M. Gomes, J. Günster, D.J. Green, Additive manufacturing of ceramics: issues, potentialities, and opportunities, J. Am. Ceram. Soc. 98 (7) (2015) 1983–2001.
[43] S. Vock, B. Klöden, A. Kirchner, T. Weißgärber, B. Kieback, Powders for powder bed fusion: a review, Prog. Addit. Manuf. 4 (4) (2019) 383–397.
[44] K. Kendall, Adhesion: molecules and mechanics, Science 263 (5154) (1994) 1720–1725.
[45] T. Krause, S. Engler, J. Gunster, J.G. Heinrich, Process and a device for producing ceramic molds, Google Patents, 2004.
[46] F. Wirth, D. Eisenbarth, K. Wegener, Absorptivity measurements and heat source modeling to simulate laser cladding, Phys. Procedia 83 (2016) 1424–1434.
[47] D.S. Thomas, S.W. Gilbert, Costs and Cost Effectiveness of Additive Manufacturing, 2014.
[48] B.P. Conner, G.P. Manogharan, A.N. Martof, L.M. Rodomsky, C.M. Rodomsky, D. C. Jordan, J.W. Limperos, Making sense of 3-D printing: creating a map of additive manufacturing products and services, Addit. Manuf. 1-4 (2014) 64–76.
[49] Print me a Stradivarius - How a new manufacturing technology will change the world, The Economist, 2011 (Accessed 17.07.2020).
[50] B. Berman, 3-D printing: the new industrial revolution, Bus. Horiz. 55 (2) (2012) 155–162.
[51] V. Petrovic, J. Vicente Haro Gonzalez, O. Jordá Ferrando, J. Delgado Gordillo, J. Ramón Blasco Puchades, L. Portolés Griñan, Additive layered manufacturing: sectors of industrial application shown through case studies, Int. J. Prod. Res. 49 (4) (2011) 1061–1079.
[52] M. Pfaffinger, G. Mitteramskogler, R. Gmeiner, J. Stampfl, Thermal debinding of ceramic-filled photopolymers, Mater. Sci. Forum 825-826 (2015) 75–81.
[53] P. Serlenga, F. Montaville, Five Questions to Shape a Winning 3-D Printing Strategy, Bain & Company, Inc., 2015 (Accessed 02.06.2020), https://www.bain.com/insights/five-questions-to-shape-a-winning-3d-printing-strategy/.
[54] M. Borlaf, A. Serra-Capdevila, C. Colominas, T. Graule, Development of UV-curable ZrO2 slurries for additive manufacturing (LCM-DLP) technology, J. Eur. Ceram. Soc. 39 (13) (2019) 3797–3803.
[55] S.H. Huang, P. Liu, A. Mokasdar, L. Hou, Additive manufacturing and its societal impact: a literature review, Int. J. Adv. Manuf. Technol. 67 (5) (2013) 1191–1203.
[56] N. Gladstone, Disadvantages of 3D Printers, https://ourpastimes.com/polaroid-vs-digital-12213612.htmlhttps://ourpastimes.com/disadvantages-of-3d-printers-12438915.html. (Accessed 17.07.2020).
[57] F. Klocke, Modern approaches for the production of ceramic components, J. Eur. Ceram. Soc. 17 (2) (1997) 457–465.
[58] P. Stoneman, The Economics of Technological Diffusion, Wiley-Blackwell, 2001.
[59] S. Mellor, L. Hao, D. Zhang, Additive manufacturing: a framework for implementation, Int. J. Prod. Econ. 149 (2014) 194–201.
[60] D. Doherty, Downloading infringement: patent law as a roadblock to the 3D printing revolution, Harvard J. Law Technol. 26 (2012) 353.
[61] H. Salmang, H. Scholze, Keramik, Springer-Verlag Berlin Heidelberg Berlin Heidelberg 2007.
[62] J.D. Cawley, Solid freeform fabrication of ceramics, Curr. Opin. Solid State Mater. Sci. 4 (5) (1999) 483–489.
[63] M. Makowska, S. Pfeiffer, N. Casati, K. Florio, M. Vetterli, K. Wegener, T. Graule, H. van Swygenhoven, Pre-processing of hematite-doped alumina granules for selective laser melting, Ceram. Int. 45 (14) (2019) 17014–17022.
[64] R.K. McGeary, Mechanical packing of spherical particles, J. Am. Ceram. Soc. 44 (10) (1961) 513–522.
[65] M. Mapar, D.Q. Zhang, Z.H. Liu, W.Y. Yeong, C.K. Chua, B.Y. Tay, O. Geramifard, S. Maleksaeedi, F.E. Wiria, Preparation and flowability characterization of ceramic powders for selective laser melting. High Value Manufacturing: Advanced Research in Virtual and Rapid Prototyping, 2014, pp. 267–271. Leira, PT.
[66] M. Mapar, Selective Laser Melting of Ceramic-Based Materials for Dental Applications, Nanyang Technological University, 2014.
[67] H. Liu, H. Su, Z. Shen, E. Wang, D. Zhao, M. Guo, J. Zhang, L. Liu, H. Fu, Direct formation of Al2O3/GdAlO3/ZrO2 ternary eutectic ceramics by selective laser melting: microstructure evolutions, J. Eur. Ceram. Soc. 38 (15) (2018) 5144–5152.
[68] Q. Liu, Y. Danlos, B. Song, B. Zhang, S. Yin, H. Liao, Effect of high-temperature preheating on the selective laser melting of yttria-stabilized zirconia ceramic, J. Mater. Process. Tech. 222 (2015) 61–74.
[69] Q. Liu, B. Song, H. Liao, Microstructure study on selective laser melting yttria stabilized zirconia ceramic with near IR fiber laser, Rapid Prototyp. J. (2014).
[70] M. Gan, C. Wong, Experimental studies on the properties of selectively laser melted alumina-spodumene composite, Ceram. Int. 44 (15) (2018) 19008–19015.
[71] H. Exner, M. Horn, A. Streek, L. Hartwig, R. Ebert, First results in laser micro sintering of ceramic materials, in: European Congress on Advanced Materials and Processes, Prague, 2005.
[72] H. Exner, M. Horn, A. Streek, F. Ullmann, L. Hartwig, P. Regenfuß, R. Ebert, Laser micro sintering: a new method to generate metal and ceramic parts of high resolution with sub-micrometer powder, Virt. Phys. Prototyping 3 (1) (2008) 3–11.
[73] P. Regenfuss, A. Streek, L. Hartwig, M. Horn, S. Klötzer, R. Ebert, H. Exner, Laser Micro Sintering of Ceramics–Reaction Models and Results, Ceramic Forum International/Ber., DKG, 2008, pp. 65–72.
[74] H. Exner, A. Streek, High resolution laser micro sintering/melting using q-switched and high brilliant laser radiation. Laser 3D Manufacturing II, International Society for Optics and Photonics, 2015, p. 93530P.
[75] J.G. Heinrich, A. Gahler, J. Günster, M. Schmücker, J. Zhang, D. Jiang, M. Ruan, Microstructural evolution during direct laser sintering in the Al2O3–SiO2 system, J. Mater. Sci. 42 (14) (2007) 5307–5311.
[76] K. Zhang, T. Liu, W. Liao, C. Zhang, Y. Yan, D. Du, Influence of laser parameters on the surface morphology of slurry-based Al2O3 parts produced through selective laser melting, Rapid Prototyping J. 24 (2) (2018) 333–341.
[77] A.M. Waetjen, D.A. Polsakiewicz, I. Kuhl, R. Telle, H. Fischer, Slurry deposition by airbrush for selective laser sintering of ceramic components, J. Eur. Ceram. Soc. 29 (1) (2009) 1–6.
[78] J. Robertson, Band offsets of wide-band-gap oxides and implications for future electronic devices, J. Vac. Sci. Technol. B 18 (3) (2000) 1785–1791.
[79] Z. Zhao, M. Mapar, W.Y. Yeong, S. Zhang, D. Zhao, Initial study of selective laser melting of ZrO2/Al2O3 ceramic, Proceedings of the 1st International Conference on Progress in Additive Manufacturing (2014).
[80] A. Henniche, J. Ouyang, Y. Ma, Z. Wang, Z. Liu, Y. Wang, M. Derradji, X. Liu, Microstructure, mechanical and thermo-physical properties of hot-pressed Al2O3-GdAlO3-ZrO2 ceramics with eutectic composition, Prog. Nat. Sci. 27 (4) (2017) 491–497.

[81] N. Coulon, P. Aubry, Results on laser sintering system for direct manufacturing of metallic or ceramic components, Int. Congr. Appl. Lasers Electro-Opt. 2004 (1) (2004) P543.
[82] N.K. Tolochko, Y.V. Khlopkov, S.E. Mozzharov, M.B. Ignatiev, T. Laoui, V.I. Titov, Absorptance of powder materials suitable for laser sintering, Rapid Prototyping J. 6 (3) (2000) 155–161.
[83] J. Wilkes, K. Wissenbach, Rapid manufacturing of ceramic components by selective laser melting. Lasers in Manufacturing, 2007, pp. 207–211. Munich.
[84] J. Wilkes, K. Wissenbach, Rapid manufacturing of ceramic components for medical and technical applications via selective laser melting, in: Conferences Euro-uRapid, Frankfurt, 2006.
[85] S. Bai, J. Liu, Femtosecond laser additive manufacturing of multi-material layered structures, Appl. Sci. 10 (3) (2020) 979.
[86] R.S. Khmyrov, C.E. Protasov, S.N. Grigoriev, A.V. Gusarov, Crack-free selective laser melting of silica glass: single beads and monolayers on the substrate of the same material, Int. J. Adv. Manuf. Technol. 85 (5) (2016) 1461–1469.
[87] R. Gmeiner, U. Deisinger, J. Schönherr, B. Lechner, R. Detsch, A. Boccaccini, J. Stampfl, Additive manufacturing of bioactive glasses and silicate bioceramics, J. Ceram. Sci. Technol 6 (2) (2015) 75–86.
[88] G. Manob, L. Lu, J. Fuh, Y. Cheng, Porous Li2O Al2O3SiO2 (LAS) glass-ceramics prepared by selective laser melting and annealing, in: 27th Annual Cocoa Beach Conference on Advanced Ceramics and Composites: B: Ceramic Engineering and Science Proceedings, Wiley Online Library, 2003, pp. 523–528.
[89] I.S. Lee, Rapid full densification of alumina-glass composites fabricated by a selective laser sintering process, J. Mater. Sci. Lett. 17 (22) (1998) 1907–1911.
[90] I. Lee, A. Manthiram, H. Marcus, Selective laser sintering of alumina-zinc borosilicate glass composites using monoclinic HB02 as a binder, 1995 International Solid Freeform Fabrication Symposium (1995).
[91] I. Lee, A. Manthiram, H. Marcus, Selective laser sintering of alumina-boron oxide composites, 1994 International Solid Freeform Fabrication Symposium (1994).
[92] B.H. Bae, J.W. Lee, J.M. Cha, I.-W. Kim, H.-D. Jung, C.-B. Yoon, Preliminary characterization of glass/alumina composite using laser powder bed fusion (L-PBF) additive manufacturing, Materials 13 (9) (2020) 2156.
[93] W. Wang, Y.X. Liu, J.Y.H. Fuh, P.J. Wang, Alumina-zirconia-Silica ceramics synthesis by selective laser sintering/melting, Appl. Mech. Mater. 121-126 (2011) 2487–2491.
[94] W. Wang, S. Ma, J. Fuh, L. Lu, Y. Liu, Processing and characterization of laser-sintered Al 2 O 3/ZrO 2/SiO 2, Int. J. Adv. Manuf. Technol. 68 (9-12) (2013) 2565–2569.
[95] I. Shishkovsky, I. Yadroitsev, P. Bertrand, I. Smurov, Alumina–zirconium ceramics synthesis by selective laser sintering/melting, Appl. Surf. Sci. 254 (4) (2007) 966–970.
[96] K. Subramanian, G. Zong, H. Marcus, Selective laser sintering and reaction sintering of ceramic composites, 1992 International Solid Freeform Fabrication Symposium (1992).
[97] A. Slocombe, L. Li, Selective laser sintering of TiC–Al2O3 composite with self-propagating high-temperature synthesis, J. Mater. Process. Tech. 118 (1) (2001) 173–178.
[98] H. Su, J. Zhang, L. Liu, J. Eckert, H. Fu, Rapid growth and formation mechanism of ultrafine structural oxide eutectic ceramics by laser direct forming, Appl. Phys. Lett. 99 (22) (2011), 221913.
[99] A.R. Thakur, J.M. Pappas, X. Dong, Fabrication and characterization of high-purity alumina ceramics doped with zirconia via laser direct deposition, JOM 72 (3) (2020) 1299–1306.
[100] J.M. Pappas, A.R. Thakur, X. Dong, Effects of zirconia doping on additively manufactured alumina ceramics by laser direct deposition, Mater. Des. (2020), 108711.
[101] D. Wu, D. Zhao, F. Niu, Y. Huang, J. Zhu, G. Ma, In situ synthesis of melt-grown mullite ceramics using directed laser deposition, J. Mater. Sci. 55 (27) (2020) 12761–12775.
[102] F. Niu, D. Wu, G. Ma, S. Zhou, B. Zhang, Effect of second-phase doping on laser deposited Al2O3 ceramics, Rapid Prototyp. J. (2015).
[103] Z. Fan, Y. Zhao, M. Lu, H. Huang, Yttria stabilized zirconia (YSZ) thin wall structures fabricated using laser engineered net shaping (LENS), Int. J. Adv. Manuf. Technol. 105 (11) (2019) 4491–4498.
[104] J.M. Pappas, E.C. Kinzel, X. Dong, Laser direct deposited transparent magnesium aluminate spinel ceramics, Manuf. Lett. (2020).
[105] J.M. Pappas, X. Dong, Porosity characterization of additively manufactured transparent MgAl2O4 spinel by laser direct deposition, Ceram. Int. 46 (5) (2020) 6745–6755.
[106] F. Niu, D. Wu, G. Ma, J. Wang, M. Guo, B. Zhang, Nanosized microstructure of Al2O3–ZrO2 (Y2O3) eutectics fabricated by laser engineered net shaping, Scr. Mater. 95 (2015) 39–41.
[107] Y. Huang, D. Wu, D. Zhao, F. Niu, H. Zhang, S. Yan, G. Ma, Process optimization of melt growth alumina/aluminum titanate composites directed energy deposition: effects of scanning speed, Addit. Manuf. (2020), 101210.
[108] G.K. Mishra, C.P. Paul, A.K. Rai, A.K. Agrawal, S.K. Rai, K.S. Bindra, Experimental investigation on Laser Directed Energy Deposition based additive manufacturing of Al2O3 bulk structures, Ceram. Int. (2020).
[109] W.J. Zhang, B.V. Reddy, S.C. Deevi, Physical properties of TiAl-base alloys, Scr. Mater. 45 (6) (2001) 645–651.
[110] F. Niu, D. Wu, S. Yan, G. Ma, B. Zhang, Process optimization for suppressing cracks in laser engineered net shaping of Al 2 O 3 ceramics, JOM 69 (3) (2017) 557–562.
[111] F. Niu, D. Wu, S. Zhou, G. Ma, Power prediction for laser engineered net shaping of Al2O3 ceramic parts, J. Eur. Ceram. Soc. 34 (15) (2014) 3811–3817.
[112] Y. Li, Y. Hu, W. Cong, L. Zhi, Z. Guo, Additive manufacturing of alumina using laser engineered net shaping: effects of deposition variables, Ceram. Int. 43 (10) (2017) 7768–7775.
[113] A. Sinhamahapatra, J.-P. Jeon, J. Kang, B. Han, J.-S. Yu, Oxygen-deficient zirconia (ZrO2−x): a new material for solar light absorption, Sci. Rep. 6 (1) (2016) 27218.
[114] Y. Waku, N. Nakagawa, T. Wakamoto, H. Ohtsubo, K. Shimizu, Y. Kohtoku, A ductile ceramic eutectic composite with high strength at 1,873 K, Nature 389 (6646) (1997) 49–52.
[115] T. Mah, T.A. Parthasarathy, L.E. Matson, Processing and mechanical properties of Al2O3/Y3Al5O12 (YAG) eutectic composite, 14th Annual Conference on Composites and Advanced Ceramic Materials: Ceramic Engineering and Science Proceedings (1990) 1617–1627.
[116] D. Wu, H. Liu, F. Lu, G. Ma, S. Yan, F. Niu, D. Guo, Al2O3-YAG eutectic ceramic prepared by laser additive manufacturing with water-cooled substrate, Ceram. Int. 45 (3) (2019) 4119–4122.
[117] F. Niu, D. Wu, G. Ma, J. Wang, J. Zhuang, Z. Jin, Rapid fabrication of eutectic ceramic structures by laser engineered net shaping, Procedia CIRP 42 (2016) 91–95.
[118] Z. Fan, Y. Zhao, Q. Tan, B. Yu, M.-X. Zhang, H. Huang, New insights into the growth mechanism of 3D-printed Al2O3–Y3Al5O12 binary eutectic composites, Scr. Mater. 178 (2020) 274–280.
[119] K. Jackson, Liquid metals and solidification, Asm, Cleveland 174 (1958).
[120] a.V.S. Stubican, R.C. Bradt, Eutectic solidification in ceramic systems, Ann. Rev. Mater. Sci. 11 (1) (1981) 267–297.
[121] P. Magnin, W. Kurz, An analytical model of irregular eutectic growth and its application to Fe-C, Acta Metall. 35 (5) (1987) 1119–1128.
[122] J.Y. Pastor, J. Llorca, P. Poza, I. de Francisco, R.I. Merino, J.I. Peña, Mechanical properties of melt-grown Al2O3–ZrO2(Y2O3) eutectics with different microstructure, J. Eur. Ceram. Soc. 25 (8) (2005) 1215–1223.
[123] J.Y. Pastor, J. LLorca, A. Salazar, P.B. Oliete, I. De Francisco, J.I. Peña, Mechanical properties of Melt-Grown Alumina–Yttrium aluminum Garnet Eutectics up to 1900 K, J. Am. Ceram. Soc. 88 (6) (2005) 1488–1495.
[124] P.B. Oliete, J.I. Peña, A. Larrea, V.M. Orera, J. LLorca, J.Y. Pastor, A. Martín, J. Segurado, Ultra-high-Strength nanofibrillar Al2O3–YAG–YSZ eutectics, Adv. Mater. 19 (17) (2007) 2313–2318.
[125] J.Y. Pastor, A. Martín, J.M. Molina-Aldareguía, J. Llorca, P.B. Oliete, A. Larrea, J. I. Peña, V.M. Orera, R. Arenal, Superplastic deformation of directionally solidified nanofibrillar Al2O3–Y3Al5O12–ZrO2 eutectics, J. Eur. Ceram. Soc. 33 (13) (2013) 2579–2586.
[126] J. Hunt, K. Jackson, Binary eutectic solidification, Trans. Metall. Soc. AIME 236 (6) (1966), 843-&.
[127] W. Kurz, D.J. Fisher, Fundamentals of Solidification, 1989.
[128] V.M. Orera, J.I. Peña, P.B. Oliete, R.I. Merino, A. Larrea, Growth of eutectic ceramic structures by directional solidification methods, J. Cryst. Growth 360 (2012) 99–104.
[129] H. Su, J. Zhang, J. Tian, L. Liu, H. Fu, Preparation and characterization of Al2O3/Y3Al5O12/ZrO2 ternary hypoeutectic in situ composites by laser rapid solidification, J. Appl. Phys. 104 (2) (2008), 023511.
[130] J. Llorca, V.M. Orera, Directionally solidified eutectic ceramic oxides, Prog. Mater. Sci. 51 (6) (2006) 711–809.
[131] J. Wang, R. Stevens, Zirconia-toughened alumina (ZTA) ceramics, J. Mater. Sci. 24 (10) (1989) 3421–3440.
[132] J.Y. Pastor, P. Poza, J. Llorca, J.I. Peña, R.I. Merino, V.M. Orera, Mechanical properties of directionally solidified Al2O3–ZrO2(Y2O3) eutectics, Mater. Sci. Eng., A 308 (1) (2001) 241–249.
[133] D. Wu, J. San, F. Niu, D. Zhao, X. Liang, S. Yan, G. Ma, Effect and mechanism of ZrO2 doping on the cracking behavior of melt-grown Al2O3 ceramics prepared by directed laser deposition, Int. J. Appl. Ceram. Technol. 17 (1) (2020) 227–238.
[134] S. Yan, D. Wu, F. Niu, Y. Huang, N. Liu, G. Ma, Effect of ultrasonic power on forming quality of nano-sized Al2O3-ZrO2 eutectic ceramic via laser engineered net shaping (LENS), Ceram. Int. 44 (1) (2018) 1120–1126.
[135] D. Wu, J. San, F. Niu, D. Zhao, Y. Huang, G. Ma, Directed laser deposition of Al 2 O 3–ZrO 2 melt-grown composite ceramics with multiple composition ratios, J. Mater. Sci. (2020) 1–16.
[136] N.P. Bansal, D. Zhu, Thermal conductivity of zirconia–alumina composites, Ceram. Int. 31 (7) (2005) 911–916.
[137] S. Yan, D. Wu, G. Ma, F. Niu, R. Kang, D. Guo, Nano-sized Al2O3-ZrO2 eutectic ceramic structures prepared by ultrasonic-assisted laser engineered net shaping, Mater. Lett. 212 (2018) 8–11.
[138] S. Yan, D. Wu, F. Niu, G. Ma, R. Kang, Al2O3-ZrO2 eutectic ceramic via ultrasonic-assisted laser engineered net shaping, Ceram. Int. 43 (17) (2017) 15905–15910.
[139] S. Yan, Y. Huang, D. Zhao, F. Niu, G. Ma, D. Wu, 3D printing of nano-scale Al2O3-ZrO2 eutectic ceramic: principle analysis and process optimization of pores, Addit. Manuf. 28 (2019) 120–126.
[140] Y. Hu, F. Ning, W. Cong, Y. Li, X. Wang, H. Wang, Ultrasonic vibration-assisted laser engineering net shaping of ZrO2-Al2O3 bulk parts: effects on crack suppression, microstructure, and mechanical properties, Ceram. Int. 44 (3) (2018) 2752–2760.
[141] D. Wu, F. Lu, D. Zhao, G. Ma, C. Li, J. Ding, F. Niu, Effect of doping SiC particles on cracks and pores of Al2O3–ZrO2 eutectic ceramics fabricated by directed laser deposition, J. Mater. Sci. 54 (13) (2019) 9321–9330.
[142] S. Yan, D. Wu, Y. Huang, N. Liu, Y. Zhang, F. Niu, G. Ma, C fiber toughening Al2O3-ZrO2 eutectic via ultrasonic-assisted directed laser deposition, Mater. Lett. 235 (2019) 228–231.

[143] Z. Liu, K. Song, B. Gao, T. Tian, H. Yang, X. Lin, W. Huang, Microstructure and mechanical properties of Al2O3/ZrO2 directionally solidified eutectic ceramic prepared by laser 3D printing, J. Mater. Sci. Technol. 32 (4) (2016) 320–325.
[144] Y. Hu, H. Wang, W. Cong, B. Zhao, Directed energy deposition of zirconia-toughened alumina ceramic: novel microstructure formation and mechanical performance, J. Manuf. Sci. Eng. 142 (2) (2020).
[145] G. Ma, S. Yan, F. Niu, Y. Zhang, D. Wu, Microstructure and mechanical properties of solid AL2O3-ZRO2 (Y2O3) eutectics prepared by laser engineered net shaping, J. Laser App. 29 (2) (2017), 022305.
[146] S. Yan, D. Wu, G. Ma, F. Niu, R. Kang, D. Guo, Formation mechanism and process optimization of nano Al2O3-ZrO2 eutectic ceramic via laser engineered net shaping (LENS), Ceram. Int. 43 (17) (2017) 14742–14747.
[147] F. Niu, D. Wu, Y. Huang, S. Yan, G. Ma, C. Li, J. Ding, Direct additive manufacturing of large-sized crack-free alumina/aluminum titanate composite ceramics by directed laser deposition, Rapid Prototyping J. (2019).
[148] D. Wu, Y. Huang, F. Niu, G. Ma, S. Yan, C. Li, J. Ding, Effects of TiO2 doping on microstructure and properties of directed laser deposition alumina/aluminum titanate composites, Virtual Phys. Prototyping 14 (4) (2019) 371–381.
[149] Y. Ohya, S. Yamamoto, T. Ban, M. Tanaka, S. Kitaoka, Thermal expansion and mechanical properties of self-reinforced aluminum titanate ceramics with elongated grains, J. Eur. Ceram. Soc. 37 (4) (2017) 1673–1680.
[150] N.P. Padture, S.J. Bennison, H.M. Chan, Flaw-tolerance and crack-resistance properties of alumina-aluminum titanate composites with tailored microstructures, J. Am. Ceram. Soc. 76 (9) (1993) 2312–2320.
[151] S. Bueno, M.-H. Berger, R. Moreno, C. Baudín, Fracture behaviour of microcrack-free alumina–aluminium titanate ceramics with second phase nanoparticles at alumina grain boundaries, J. Eur. Ceram. Soc. 28 (10) (2008) 1961–1971.
[152] S. Kanzaki, H. Tabata, T. Kumazawa, S. Ohta, Sintering and mechanical properties of stoichiometric mullite, J. Am. Ceram. Soc. 68 (1) (1985) C-6–C-7.
[153] W.E. Cameron, Mullite; a substituted alumina, Am. Mineral. 62 (7-8) (1977) 747–755.
[154] H. Schneider, R.X. Fischer, J. Schreuer, Mullite: crystal structure and related properties, J. Am. Ceram. Soc. 98 (10) (2015) 2948–2967.
[155] R.G. Carvalho, A.J.S. Fernandes, F.J. Oliveira, E. Alves, N. Franco, C. Louro, R. F. Silva, F.M. Costa, Single and polycrystalline mullite fibres grown by laser floating zone technique, J. Eur. Ceram. Soc. 30 (16) (2010) 3311–3318.
[156] F. Li, Y. Zhang, Microstructural characterization of Al2O3-ZrO2 ceramic by laser direct material deposition, J. Laser App. 31 (2) (2019), 022509.
[157] F. Li, X. Zhang, C. Sui, J. Wu, H. Wei, Y. Zhang, Microstructure and mechanical properties of Al2O3-ZrO2 ceramic deposited by laser direct material deposition, Ceram. Int. 44 (15) (2018) 18960–18968.
[158] W. Duckworth, Discussion of ryshkewitch paper by winston duckworth, J. Am. Ceram. Soc. 36 (1953) 68.
[159] A. Standard, Standard Test Methods for Apparent Porosity, Water Absorption, Apparent Specific Gravity, and Bulk Density of Burned Refractory Brick and Shapes by Boiling Water, West Conshohocken, PA.: ASTM C20-00, 2015.
[160] J. Wilkes, K. Wissenbach, Rapid manufacturing of cermic components by selective laser melting, in: Fourth International WLT-Conference on Lasers in Manufacturing, Munich, 2007, pp. 207–211.
[161] W. Kurz, D.J. Fisher, Dendrite growth in eutectic alloys: the coupled zone, Int. Met. Rev. 24 (1) (1979) 177–204.
[162] W. Kurz, R. Trivedi, Rapid solidification processing and microstructure formation, Mater. Sci. Eng., A 179-180 (1994) 46–51.
[163] G.D. Quinn, R.C. Bradt, On the vickers indentation fracture toughness test, J. Am. Ceram. Soc. 90 (3) (2007) 673–680.
[164] J.I. Wilkes, Selektives Laserschmelzen zur generativen Herstellung von Bauteilen aus hochfester Oxidkeramik, RWTH Aachen, 2009.
[165] Y.-C. Hagedorn, Additive Manufacturing of High Performance Oxide Ceramics Via Selective Laser Melting, RWTH Aachen, 2013.
[166] K. Shimizu, M. Oka, P. Kumar, Y. Kotoura, T. Yamamuro, K. Makinouchi, T. Nakamura, Time-dependent changes in the mechanical properties of zirconia ceramic, J. Biomed. Mater. Res. 27 (6) (1993) 729–734.
[167] A.V. Gusarov, I.S. Malakhova-Ziablova, M.D. Pavlov, Thermoelastic residual stresses and deformations at laser treatment, Phys. Procedia 41 (2013) 896–903.
[168] A.V. Gusarov, M. Pavlov, I. Smurov, Residual stresses at laser surface remelting and additive manufacturing, Phys. Procedia 12 (2011) 248–254.
[169] M. Yamane, J.D. Mackenzie, Vicker's hardness of glass, J. Non-Cryst. Solids 15 (2) (1974) 153–164.
[170] A. Krell, P. Blank, Grain size dependence of hardness in dense submicrometer alumina, J. Am. Ceram. Soc. 78 (4) (1995) 1118–1120.
[171] G.N. Morscher, P. Pirouz, A.H. Heuer, Temperature dependence of hardness in yttria-stabilized zirconia single crystals, J. Am. Ceram. Soc. 74 (3) (1991) 491–500.
[172] X. Teng, H. Liu, C. Huang, Effect of Al2O3 particle size on the mechanical properties of alumina-based ceramics, Mater. Sci. Eng., A 452-453 (2007) 545–551.
[173] J.I. Peña, M. Larsson, R.I. Merino, Id. Francisco, V.M. Orera, J. Llorca, J.Y. Pastor, A. Martín, J. Segurado, Processing, microstructure and mechanical properties of directionally-solidified Al2O3–Y3Al5O12–ZrO2 ternary eutectics, J. Eur. Ceram. Soc. 26 (15) (2006) 3113–3121.
[174] L. Caprio, A.G. Demir, B. Previtali, B.M. Colosimo, Determining the feasible conditions for processing lunar regolith simulant via laser powder bed fusion, Addit. Manuf. 32 (2020), 101029.
[175] M. Mani, B.M. Lane, M.A. Donmez, S.C. Feng, S.P. Moylan, A review on measurement science needs for real-time control of additive manufacturing metal powder bed fusion processes, Int. J. Prod. Res. 55 (5) (2017) 1400–1418.
[176] S.K. Everton, M. Hirsch, P. Stravroulakis, R.K. Leach, A.T. Clare, Review of in-situ process monitoring and in-situ metrology for metal additive manufacturing, Mater. Des. 95 (2016) 431–445.
[177] B.M. Colosimo, M. Grasso, In-situ monitoring in L-PBF: opportunities and challenges, Procedia CIRP 94 (2020) 388–391.
[178] M. Grasso, B.M. Colosimo, Process defects andin situmonitoring methods in metal powder bed fusion: a review, Meas. Sci. Technol. 28 (4) (2017), 044005.
[179] V. Renken, A. von Freyberg, K. Schünemann, F. Pastors, A. Fischer, In-process closed-loop control for stabilising the melt pool temperature in selective laser melting, Prog. Addit. Manuf. 4 (4) (2019) 411–421.
[180] E. Vasileska, A.G. Demir, B.M. Colosimo, B. Previtali, Layer-wise control of selective laser melting by means of inline melt pool area measurements, J. Laser App. 32 (2) (2020), 022057.
[181] B.M. Colosimo, E. Grossi, F. Caltanissetta, M. Grasso, Penelope: A Novel Prototype for In Situ Defect Removal in LPBF, JOM 72 (3) (2020) 1332–1339.
[182] D. Puccio, Selective Laser Melting of Alumina : Process Capability and Monitoring, Politecnico di Milano, 2019 master thesis.
[183] L. Lacertosa, In-situ Monitoring and Ex-situ Measurements on Selective Laser Melting of Ceramic Materials, Politecnico di Milano, 2019 master thesis.
[184] B. Qian, L. Taimisto, A. Lehti, H. Piili, O. Nyrhilä, A. Salminen, Z. Shen, Monitoring of temperature profiles and surface morphologies during laser sintering of alumina ceramics, J. Asian Ceram. Soc. 2 (2) (2014) 123–131.
[185] K. Zhang, T. Liu, W. Liao, C. Zhang, D. Du, Y. Zheng, Photodiode data collection and processing of molten pool of alumina parts produced through selective laser melting, Optik 156 (2018) 487–497.
[186] G. Repossini, V. Laguzza, M. Grasso, B.M. Colosimo, On the use of spatter signature for in-situ monitoring of Laser Powder Bed Fusion, Addit. Manuf. 16 (2017) 35–48.
[187] Arcam AB – the innovative leader in additive manufacturing solutions for the production of orthopedic implants and aerospace components, 2016. (Accessed 04.01.2021).
[188] A. Klimov, I.Y. Bakeev, E. Dvilis, E. Oks, A. Zenin, Electron beam sintering of ceramics for additive manufacturing, Vacuum 169 (2019), 108933.
[189] D. Eisenbarth, F. Soffel, K. Wegener, Geometry-Based Process Adaption to Fabricate Parts With Varying Wall Thickness by Direct Metal Deposition, Springer International Publishing, Cham, 2020, pp. 125–130.
[190] H.P. Cahoon, C.J. Christensen, Sintering and grain growth of alpha-alumina, J. Am. Ceram. Soc. 39 (10) (1956) 337–344.
[191] R. Raman, S. Rele, R. Anderson, Potential application of solid free-form fabrication (SFF) process in ceracon P/M forging, 1993 International Solid Freeform Fabrication Symposium (1993).
[192] M. Schmücker, P. Mechnich, All-oxide ceramic matrix composites with porous matrices, in: W. Krenkel (Ed.), Ceramic Matrix Composites: Fiber Reinforced Ceramics and Their Applications, WILEY-VCH Verlag GmbH & Co., Weinheim, 2008.
[193] G. Jefferson, K.A. Keller, R.S. Hay, R.J. Kerans, Oxide/oxide composites with fiber coatings, in: W. Krenkel (Ed.), Ceramic Matrix Composites: Fiber Reinforced Ceramics and Their Applications, WILEY-VCH Verlag GmbH & Co, Weinheim, 2008.
[194] J.F. Li, L. Li, F.H. Stott, Thermal stresses and their implication on cracking during laser melting of ceramic materials, Acta Mater. 52 (14) (2004) 4385–4398.
[195] Q. Chen, G. Guillemot, C.-A. Gandin, M. Bellet, Numerical modelling of the impact of energy distribution and Marangoni surface tension on track shape in selective laser melting of ceramic material, Addit. Manuf. 21 (2018) 713–723.
[196] Q. Chen, G. Guillemot, C.-A. Gandin, M. Bellet, Three-dimensional finite element thermomechanical modeling of additive manufacturing by selective laser melting for ceramic materials, Addit. Manuf. 16 (2017) 124–137.
[197] T. Heeling, M. Cloots, K. Wegener, Melt pool simulation for the evaluation of process parameters in selective laser melting, Addit. Manuf. 14 (2017) 116–125.
[198] J. Weirather, V. Rozov, M. Wille, P. Schuler, C. Seidel, N.A. Adams, M.F. Zaeh, A smoothed particle hydrodynamics model for laser beam melting of Ni-based alloy 718, Comput. Math. Appl. 78 (7) (2019) 2377–2394.
[199] M.A. Russell, A. Souto-Iglesias, T.I. Zohdi, Numerical simulation of laser fusion additive manufacturing processes using the SPH method, Comput. Methods Appl. Mech. Eng. 341 (2018) 163–187.